

THREE LECTURES ON MULTI-PARTICLE  
PRODUCTION IN THE GLASMA\*

FRANÇOIS GELIS,

CEA, Service de Physique Théorique (URA 2306 du CNRS)  
91191, Gif-sur-Yvette Cedex, France

RAJU VENUGOPALAN

Brookhaven National Laboratory, Department of Physics  
Bldg. 510 A Upton, NY-11973, USA*(Received November 13, 2006)*

In the Color Glass Condensate (CGC) effective field theory, when two large sheets of Colored Glass collide, as in a central nucleus–nucleus collision, they form a strongly interacting, non-equilibrium state of matter called the Glasma. How Colored Glass shatters to form the Glasma, the properties of the Glasma, and the complex dynamics transforming the Glasma to a thermalized Quark Gluon Plasma (QGP) are questions of central interest in understanding the properties of the strongly interacting matter produced in heavy ion collisions. In the first of these lectures, we shall discuss how these questions may be addressed in the framework of particle production in a field theory with strong time dependent external sources. Albeit such field theories are non-perturbative even for arbitrarily weak coupling, moments of the multiplicity distribution can in principle be computed systematically in powers of the coupling constant. We will demonstrate that the average multiplicity can be (straightforwardly) computed to leading order in the coupling and (remarkably) to next-to-leading order as well. The latter are obtained from solutions of small fluctuation equations of motion with *retarded boundary conditions*. In the second lecture, we relate our formalism to results from previous 2+1 and 3+1 dimensional numerical simulations of the Glasma fields. The latter show clearly that the expanding Glasma is unstable; small fluctuations in the initial conditions grow exponentially with the square root of the proper time. Whether this explosive growth of small fluctuations leads to early thermalization in heavy ion collisions requires at present a better understanding of these fluctuations on the light cone. In the third and final lecture, motivated by recent work A. Bialas, M. Jeżabek, *Phys. Lett. B* **590**, 233 (2004), we will discuss how the widely observed phenomenon of limiting fragmentation is realized in the CGC framework.

PACS numbers: 12.38.–t, 12.38.Mh, 25.75.Nq

---

\* Presented at the XLVI Cracow School of Theoretical Physics, Zakopane, Poland May 27–June 5, 2006.

## 1. Introduction

The theme of these lectures at the XLVI course of the Zakopane school is multi-particle production in hadronic collisions at high energies in the Color Glass Condensate (CGC) effective field theory. There has been tremendous progress in our theoretical understanding in the seven years since one of the authors last lectured here. At that time, the author's lectures covered the state of the art (in the CGC framework) in both deeply inelastic scattering (DIS) studies and in hadronic multi-particle production [2]. A sign of rapid progress in the field is that there were several talks and lectures at this school covering various aspects of this physics in DIS alone. We will restrict ourselves here to developments in our understanding of multi-particle production in hadronic collisions. Another significant development in the last seven years has been the large amount of data from the Relativistic Heavy Ion Collider (RHIC) at BNL, key features of which were nicely summarized in the white-papers of the experimental collaborations [3] culminating in the announcement of the discovery of a “perfect fluid” at RHIC. The exciting experimental observations were discussed here in the lectures of Jacak [4]. The RHIC data have had a tremendous impact on the CGC studies of multi-particle production. While we will discuss RHIC phenomenology, and indeed specific applications of theory to data, our primary focus will be on attempts to develop a systematic theoretical framework in QCD to compute multi-particle production in hadronic collisions. Some applications of the CGC approach to RHIC phenomenology were also covered at this school by Kharzeev as part of his lectures [5]. For recent comprehensive reviews, see Ref. [6, 7].

The collider era in high energy physics has made possible investigations of QCD structure at a deep level in studies of multi-particle final states. Much attention has been focused on the nature of multi-particle production in jets; for a nice review, see Refs. [8, 9]. The problem is, however, very general. Theoretical developments in the last couple of decades suggest that semi-hard particle production in high energy hadronic interactions is dominated by interactions between partons having a small fraction  $x$  of the longitudinal momentum of the incoming nucleons. In the Regge limit of small  $x$  and fixed momentum transfer squared  $Q^2$  (corresponding to very large center of mass energies  $\sqrt{s}$ ) the Balitsky–Fadin–Kuraev–Lipatov (BFKL) evolution equation [10, 11] predicts that parton densities grow very rapidly with decreasing  $x$ . A rapid growth with  $x$ , in the gluon distribution, for fixed  $Q^2 \gg \Lambda_{\text{QCD}}^2$ , was observed in the HERA experiments [12, 13]. (It is not clear however that the observed growth of the gluon distribution is a consequence of BFKL dynamics [14].) Because the rapid growth in the Regge limit corresponds to very large phase space densities of partons in hadronic

wave functions, saturation effects may play an important role in hadronic collisions at very high energies [15–18]. These slow down the growth of parton densities relative to that of BFKL evolution and may provide the mechanism for the unitarization of cross-sections at high energies.

The large parton phase space density suggests that small  $x$  partons can be described by a classical color field rather than as particles [19–21]. Light cone kinematics (more simply, time dilation) further indicates that there is a natural separation in time scales, whereby the small  $x$  partons are the dynamical degrees of freedom and the large  $x$  partons act as static color sources for the classical field. In the McLerran–Venugopalan (MV) model, the large color charge density of sources is given by the density of large  $x$  partons in a big nucleus which contains  $3A$  valence quarks (where  $A$  is the atomic number of the nucleus). In this limit of strong color sources, one has to solve the non-linear classical Yang–Mills equations to obtain the classical field corresponding to the small  $x$  parton modes. This procedure properly incorporates, at tree level, the recombination interactions that are responsible for gluon saturation. In the MV model, the distribution of large  $x$  color sources is described by a Gaussian statistical distribution [19, 22]. A more general form of this statistical distribution, for  $SU(N_c)$  gauge theories, valid for large  $A$  and moderate  $x$ , is given in Refs. [23, 24].

The separation between large  $x$  and small  $x$ , albeit natural, is somewhat arbitrary in the MV model; the physics should in fact be independent of this separation of scales. This property was exploited to derive a functional renormalization group (RG) equation, the JIMWLK equation, describing the evolution of the gauge invariant source distributions to small  $x$  [25–32]. The JIMWLK functional RG equation is equivalent to an infinite hierarchy of evolution equations describing the behavior of multi-parton correlations at high energies first derived by Balitsky [33]. A useful (and tremendously simpler) large  $N_c$  and large  $A$  mean-field approximation independently derived by Kovchegov [34], is commonly known as the Balitsky–Kovchegov equation. The general effective field theory framework describing the non-trivial behavior of multi-parton correlations at high energies is often referred to as the Color Glass Condensate (CGC) [35–37].

Several lecturers at the school discussed the state of the art in our understanding of the small  $x$  wavefunction [38]. For previous discussions at recent schools, see Refs. [39–41]. To compute particle production in the CGC framework, in addition to knowing the distribution of sources in the small  $x$  nuclear wavefunction, one must calculate the properties of multi-particle production for any particular configuration of sources. In this paper, we will assume that the former is known. All we require is that these sources (as the RG equations tell us) are strong sources, parametrically of the order of the inverse coupling constant, and are strongly time dependent. We will

describe a formalism to compute multi-particle production for an arbitrary distribution of such sources<sup>1</sup>.

These lectures are organized as follows. In the first lecture, we shall describe the formalism for computing particle production in a field theory coupled to strong time-dependent external classical sources. We will consider as a toy model a  $\phi^3$  scalar theory, where  $\phi$  is coupled to a strong external source. Although the complications of QCD — such as gauge invariance — are very important, many of the lessons gained from this simpler scalar theory apply to studies of particle production in QCD. We will demonstrate that there is no simple power counting in the coupling constant  $g$  for the probability  $P_n$  to produce  $n$  particles. A simple power counting however exists for moments of  $P_n$ . We will discuss how one computes the average multiplicity and (briefly) the variance. With regard to the former, we will show how it can be computed to next-to-leading order in the multiplicity. We will also discuss what it takes to compute the generating function for the multiplicity distribution to leading order in the coupling.

In lecture II, we will relate the formal considerations developed in lecture I, to the results of real time numerical simulations of the average multiplicity of gluons and quarks produced in heavy ion collisions. Inclusive gluon production, to lowest order in the loop expansion discussed in lecture I, is obtained by solving the classical Yang–Mills equations for two color sources moving at the speed of light in opposite directions [42–44]. This problem has been solved numerically in [45–50] for the boost-invariant case. The multiplicity of quark-pairs is computed from the quark propagator in the background field of [45–50] — it has been studied numerically in [51, 52]. A first computation for the boost non-invariant case has also been performed recently [53, 54]. It was shown there that rapidity dependent fluctuations of the classical fields lead to the non-Abelian analog of the Weibel instability [55], first studied in the context of electromagnetic plasmas. Such instabilities may be responsible for the early thermalization required by phenomenological studies of heavy ion collisions. We will discuss how a better understanding of the small quantum fluctuations discussed in lecture I may provide insight into early thermalization.

In the third and final lecture, we will discuss how the formalism outlined in lecture I simplifies in the case of proton–nucleus collisions. (A similar simplification occurs in hadron–hadron collisions at forward/backward rapidities where large  $x$ ’s in one hadron (small color charge density) and small  $x$  in the other (large color charge density) are probed.) At leading order in the coupling, lowest order in the proton charge density, and all orders in the nuclear

---

<sup>1</sup> That one can separate the properties of partons in the wave function from those in the final state is a statement of factorization. This has not yet been proven. We will briefly describe work in that direction in these lectures.

color charge density, analytical results are available for both inclusive gluon and quark production<sup>2</sup>. In the former case, the analytical formula can be written, in  $k_\perp$  factorized form, as the product of unintegrated distributions in both the proton and the nucleus convoluted with the matrix element for the interactions squared. This formula is used extensively in the literature for phenomenological applications. We will discuss one such application, that of limiting fragmentation.

## 2. Lecture I: How Colored Glass shatters to form the Glasma

As outlined in the introduction, the Glasma is formed when two sheets of Colored Glass collide, producing a large number of partons. A cartoon depicting this collision is shown in Fig. 1. In the CGC framework, it is

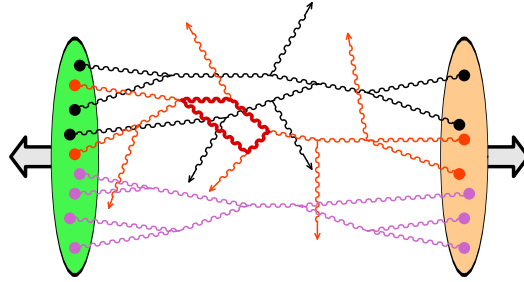


Fig. 1. Typical contribution to gluon production in the collision of two sheets of Colored Glass. The dots denote the color sources that describe the fast partons in the CGC framework.

expected that observables can be expressed as<sup>3</sup>

$$\langle \mathcal{O} \rangle_Y = \int [D\rho_1] [D\rho_2] W_{Y_{\text{beam}}-Y}[\rho_1] W_{Y_{\text{beam}}+Y}[\rho_2] \mathcal{O}[\rho_1, \rho_2], \quad (1)$$

where they are first computed as a functional of the color charge densities  $\rho_1$  and  $\rho_2$  of the two nuclei and then averaged over all possible configurations of these sources, with the likelihood of a particular configuration at a given rapidity  $Y$  ( $= \ln(1/x)$ ) specified by the weight functionals  $W_{Y_{\text{beam}}-Y}[\rho_1]$  and  $W_{Y_{\text{beam}}+Y}[\rho_2]$  respectively. Here  $Y_{\text{beam}} = \frac{1}{2} \ln(s/m_p^2)$  is the beam rapidity in a hadronic collision ( $m_p$  denoting the proton mass) with the center of mass energy  $\sqrt{s}$ .

<sup>2</sup> For quark production,  $k_\perp$  factorization breaks down even at leading order in  $pA$  collisions [117].

<sup>3</sup> As we shall see in lecture II, this formula may also require an average over some quantum fluctuations, because of an instability in boost invariant classical solutions of the Yang-Mills equations.

The evolution of the  $W_Y[\rho]$ 's with rapidity is described by the JIMWLK equation [25–32]. For small  $x$  (large  $Y$ ) and/or large nuclei, the rapid growth of parton densities corresponds to light cone source densities  $\rho_1, \rho_2 \sim 1/g$  — in other words, the sources are strong. Thus understanding how two sheets of Colored Glass shatter to produce the Glasma requires that we understand the nature of particle production in a field theory with strong, time dependent sources. In this lecture, we will outline the tools to systematically compute particle production in such theories. More details can be found in Refs. [56, 57].

Field theories with strong time dependent sources are different from field theories in the vacuum in one key respect. The “vacuum” in the former, even in weak coupling, is non-trivial because it can produce particles. Specifically, the amplitude from the vacuum state  $|0_{\text{in}}\rangle$  to a populated state  $|\alpha_{\text{out}}\rangle$  is

$$\langle \alpha_{\text{out}} | 0_{\text{in}} \rangle \neq 0. \quad (2)$$

Unitarity requires that the sum over all “out” states satisfies the identity

$$\sum_{\alpha} \left| \langle \alpha_{\text{out}} | 0_{\text{in}} \rangle \right|^2 = 1. \quad (3)$$

We therefore conclude that

$$\left| \langle 0_{\text{out}} | 0_{\text{in}} \rangle \right|^2 < 1. \quad (4)$$

In other words, the probability that the vacuum stays empty is strictly smaller than unity. Following the conventions of [63], we can write the vacuum-to-vacuum transition amplitude as

$$\langle 0_{\text{out}} | 0_{\text{in}} \rangle \equiv e^{i\mathcal{V}[\rho]}, \quad (5)$$

where  $i\mathcal{V}[\rho]$  compactly represents the sum of the connected vacuum–vacuum diagrams in the presence of the external (in our case, strong, time dependent, colored) source  $\rho$ . Therefore, the inequality (4) means that vacuum–vacuum diagrams have a non-zero imaginary part, since  $\left| \langle 0_{\text{out}} | 0_{\text{in}} \rangle \right|^2 = \exp(-2 \text{Im } \mathcal{V}[\rho])$ . In stark contrast, for a field theory without external sources, Eq. (4) would be an equality, and the vacuum–vacuum diagrams would be purely real, thereby only giving a pure phase for the vacuum-to-vacuum amplitude in Eq. (5). They therefore do not contribute to the probabilities for producing particles.

Eq. (4) tells us that one has to be more careful in field theories with external sources. To illustrate how particle production works in such theories, we shall, for simplicity, consider a real scalar field with cubic self-interactions,

coupled to an external source. (The lessons we draw carry over straightforwardly to QCD albeit their implementation is in practice significantly more complex.) The Lagrangian density is

$$\mathcal{L} \equiv \frac{1}{2} \partial_\mu \phi \partial^\mu \phi - \frac{1}{2} m^2 \phi^2 - \frac{g}{3!} \phi^3 + \rho \phi. \quad (6)$$

Note that the coupling  $g$  in this theory has dimensions of the mass; and that the theory is super-renormalizable in  $n = 4$  dimensions. The source densities  $\rho(x)$  can be envisioned as the scalar analogue of the sum of two source terms  $\rho(x) = \rho_1(x) + \rho_2(x)$  corresponding respectively in the CGC framework to the recoil-less color currents of the two hadronic projectiles.

Let us now consider how the perturbative expansion for such a theory looks like in weak coupling. The power of a generic simply connected diagram is given simply by

$$g^{n_E + 2(n_L - 1)} (g\rho)^{n_\rho}, \quad (7)$$

where  $n_E$  are the number of external lines,  $n_L$  the number of loops and  $n_\rho$  the number of sources. For vacuum–vacuum graphs,  $n_E = 0$ . As  $\rho \sim 1/g$ , the power counting for a theory with strong sources is given entirely by an expansion in the number of loops. In particular, at tree level ( $n_L = 0$ ), the vacuum–vacuum graphs are all of order  $1/g^2$ . The tree graphs contributing to the connected vacuum–vacuum amplitude in Eq. (4) can be represented as

$$i\mathcal{V}[j] \equiv i \sum_{\text{conn}} V = \frac{1}{2} \text{---}\bullet\text{---} + \frac{1}{6} \text{---}\bullet\text{---}\begin{array}{c} \bullet \\ \diagup \quad \diagdown \\ \bullet \quad \bullet \end{array} + \frac{1}{8} \begin{array}{c} \bullet \quad \bullet \\ \diagdown \quad \diagup \\ \bullet \quad \bullet \end{array} + \frac{1}{8} \begin{array}{c} \bullet \quad \bullet \quad \bullet \\ \diagdown \quad \diagup \quad \diagdown \\ \bullet \quad \bullet \quad \bullet \end{array} + \dots \quad (8)$$

There are also loop contributions in this expression which we have not represented here.

To proceed with the perturbative computation, we need to consider the analog of the well known Cutkosky rules for this case. For each diagram in the computation, begin by assigning for each vertex and source, two kinds of vertices denoted by  $+$  or  $-$ . A vertex of type  $+$  is the ordinary vertex and appears with a factor  $-ig$  in Feynman diagrams. A vertex of type  $-$  is the opposite<sup>4</sup> of a  $+$  vertex, and its Feynman rule is  $+ig$ . Likewise, for insertions of the source  $\rho$ , insertions of type  $+$  appear with the factor  $+i\rho(x)$  while insertions of type  $-$  appear instead with  $-i\rho(x)$ . Thus for each Feynman diagram  $iV$  in Eq. (6), containing only  $+$  vertices and sources (denoted henceforth as  $iV_{\{+,\dots,+\}}$ ) contributing to the sum of connected vacuum–vacuum

<sup>4</sup> Because the coupling constant  $g$  is real in an unitary theory, the vertex of type  $-$  is also the complex conjugate of the vertex of type  $+$ .

diagrams, we obtain a corresponding set of diagrams  $iV_{\{\epsilon_i\}}$  by assigning the symbol  $\epsilon_i = \pm$  to the vertex  $i$  of the original diagram (and connecting a vertex of type  $\epsilon$  to a vertex of type  $\epsilon'$  with a propagator  $G_{\epsilon\epsilon'}^0$  — to be discussed further shortly).

The generalized set of diagrams therefore includes  $2^n$  such diagrams if the original diagram had  $n$  vertices and sources. Using recursively the so-called “largest time equation” [58, 59], one obtains the identity,

$$iV_{\{+\dots+\}} + iV_{\{-\dots-\}} = -2\text{Im } V = - \sum_{\{\epsilon_i\}'} iV_{\{\epsilon_i\}}, \quad (9)$$

where the prime in the sum means that we sum over all the combinations of  $\epsilon_i$ ’s, except the two terms where the vertices and sources are all of type  $+$  or all of type  $-$ . (There are, therefore,  $2^n - 2$  terms in this sum.)

We now need to specify the propagators connecting the  $\pm$  vertices and sources. The usual Feynman (time-ordered) free propagator is the propagator connecting two vertices of type  $+$ , *i.e.*  $G_{++}^0$ . It can be decomposed as

$$G_{++}^0(x, y) \equiv \theta(x^0 - y^0) G_{-+}^0(x, y) + \theta(y^0 - x^0) G_{+-}^0(x, y), \quad (10)$$

which defines the propagators  $G_{-+}^0$  and  $G_{+-}^0$ . Likewise, the anti-time-ordered free propagator  $G_{--}^0$  is defined as<sup>5</sup>

$$G_{--}^0(x, y) \equiv \theta(x^0 - y^0) G_{+-}^0(x, y) + \theta(y^0 - x^0) G_{-+}^0(x, y). \quad (11)$$

The Fourier transforms of the free propagators  $G_{\epsilon\epsilon'}^0$  for our scalar theory are

$$\begin{aligned} G_{++}^0(p) &= \frac{i}{p^2 - m^2 + i\epsilon}, & G_{--}^0(p) &= \frac{-i}{p^2 - m^2 - i\epsilon}, \\ G_{-+}^0(p) &= 2\pi\theta(p^0)\delta(p^2 - m^2), & G_{+-}^0(p) &= 2\pi\theta(-p^0)\delta(p^2 - m^2). \end{aligned} \quad (12)$$

For a given term in the right hand side of Eq. (9), one can divide the diagram in several regions, each containing only  $+$  or only  $-$  vertices and sources. (There is at least one external source in each of these regions because of energy conservation constraints.) The  $+$  regions and  $-$  regions of the diagram are separated by a “cut”, and one thus obtains a “cut vacuum–vacuum diagram”. At tree level, the first terms generated by these cutting rules (applied to compute the imaginary part of the sum of connected

<sup>5</sup> The notations for the propagators are those that appear in the Schwinger–Keldysh formalism developed initially for field theories at finite temperature (see [64, 65]). This identification, as we shall see later, is not accidental. The propagators so defined are not independent; they are related by the identity  $G_{++}^0 + G_{--}^0 = G_{-+}^0 + G_{+-}^0$ .



vacuum–vacuum diagrams in Eq. (9)) are

$$\begin{aligned}
 2 \operatorname{Im} \sum_{\text{conn}} V &= \frac{1}{2} \text{diagram 1} + \frac{1}{2} \text{diagram 2} \\
 &+ \frac{1}{6} \text{diagram 3} + \frac{1}{6} \text{diagram 4} + \frac{1}{6} \text{diagram 5} + \frac{1}{6} \text{diagram 6} + \frac{1}{6} \text{diagram 7} + \frac{1}{6} \text{diagram 8} \\
 &+ \frac{1}{6} \text{diagram 9} + \frac{1}{6} \text{diagram 10} + \frac{1}{6} \text{diagram 11} + \frac{1}{6} \text{diagram 12} + \frac{1}{6} \text{diagram 13} + \frac{1}{6} \text{diagram 14} \\
 &+ \dots \\
 &\equiv \frac{1}{g^2} \sum_r b_r.
 \end{aligned} \tag{13}$$

The  $+$  and  $-$  signs adjacent to the grey line in each diagram here indicate the side on which the set of  $+$  and  $-$  vertices is located. As one can see, there are cuts intercepting more than one propagator. The sum of the diagrams with  $r$  cut propagators is denoted by  $b_r/g^2$  — the identity in Eq. (13) (and Eq. (9)) is a statement of unitarity. These  $b_r$  are sometimes called “combinants” in the literature [60].

It is important to note that cut connected vacuum–vacuum diagrams would be zero in the vacuum because energy cannot flow from one side of the cut to the other in the absence of external sources. This is of course consistent with a pure phase in Eq. (9). This constraint on the energy flow is removed if the fields are coupled to *time-dependent* external sources. Cut vacuum–vacuum diagrams, and therefore the imaginary part of vacuum–vacuum diagrams, differ from zero in this case.

We now turn to the probabilities for producing  $n$  particles. The probability to produce one particle from the vacuum can be parameterized as

$$P_1 = e^{-\frac{1}{g^2} \sum_r b_r} \frac{b_1}{g^2}, \tag{14}$$

where  $b_1$ , a series in  $g^{2n}$  ( $n \geq 0$ ) is obtained by summing the 1-particle cuts through connected vacuum–vacuum diagrams. The exponential prefactor is the square of the sum of all the vacuum–vacuum diagrams, which arises in any transition probability. The probability  $P_2$  for producing two particles from the vacuum contains two pieces. One is obtained by squaring the  $b_1/g^2$  piece of the probability for producing one particle (dividing by 2 for identical particles) — in this case, the two particles are produced independently from one another. The other  $b_2/g^2$  is a “correlated” contribution from a 2-particle cut through connected vacuum–vacuum diagrams. We therefore obtain

$$P_2 = e^{-\frac{1}{g^2} \sum_r b_r} \left[ \frac{1}{2!} \frac{b_1^2}{g^4} + \frac{b_2}{g^2} \right]. \tag{15}$$

In a similar vein, the probability  $P_3$  can be shown to consist of three pieces. One (“uncorrelated”) term is the cube of  $b_1/g^2$  (preceded by a symmetry factor  $1/3!$ ). Another is the combination  $b_1b_2/g^4$ , corresponding to the production of two particles in the same subdiagram with the third produced independently from the first two. Finally, there is the “correlated” three particle production probability  $b_3/g^2$  corresponding to the production of three particles from the same diagram. The sum of these three pieces is thus

$$P_3 = e^{-\frac{1}{g^2} \sum_r b_r} \left[ \frac{1}{3!} \frac{b_1^3}{g^6} + \frac{b_1 b_2}{g^4} + \frac{b_3}{g^2} \right]. \quad (16)$$

Some of the graphs contributing to  $b_1$ ,  $b_2$  and  $b_3$  are shown in Fig. 2. Following this line of inductive reasoning, one obtains a general formula

$$\begin{aligned} \frac{b_1}{g^2} &= \frac{1}{2} \text{---} \text{---} \text{---} + \frac{1}{2} \text{---} \text{---} \text{---} \\ &+ \frac{1}{6} \text{---} \text{---} \text{---} + \frac{1}{6} \text{---} \text{---} \text{---} + \frac{1}{6} \text{---} \text{---} \text{---} + \frac{1}{6} \text{---} \text{---} \text{---} + \frac{1}{6} \text{---} \text{---} \text{---} + \frac{1}{6} \text{---} \text{---} \text{---} \\ &+ \dots \\ \frac{b_2}{g^2} &= \frac{1}{6} \text{---} \text{---} \text{---} + \frac{1}{6} \text{---} \text{---} \text{---} + \frac{1}{6} \text{---} \text{---} \text{---} + \frac{1}{6} \text{---} \text{---} \text{---} + \frac{1}{6} \text{---} \text{---} \text{---} + \frac{1}{6} \text{---} \text{---} \text{---} \\ &+ \dots \\ \frac{b_3}{g^2} &= \frac{1}{8} \text{---} \text{---} \text{---} + \frac{1}{8} \text{---} \text{---} \text{---} + \frac{1}{8} \text{---} \text{---} \text{---} \\ &+ \dots \end{aligned}$$

Fig. 2. Examples of cut diagrams contributing to  $b_1$ ,  $b_2$  and  $b_3$ .

for the production of  $n$  particles

$$P_n = e^{-\frac{1}{g^2} \sum_r b_r} \sum_{p=0}^n \frac{1}{p!} \sum_{\alpha_1 + \dots + \alpha_p = n} \frac{b_{\alpha_1} \dots b_{\alpha_p}}{g^{2p}} \quad (17)$$

for any  $n$ . In this formula,  $p$  is the number of disconnected subdiagrams producing the  $n$  particles, and  $b_r/g^2$  denotes the sum of all  $r$ -particle cuts through the connected vacuum–vacuum diagrams. This formula gives the probability of producing  $n$  particles to all orders in the coupling  $g$  in a field theory with strong external sources. It is important to realize that all the details of the dynamics of the theory under consideration are hidden in

the numbers  $b_r$ , and that Eq. (17) is a generic form for transition probabilities when many disconnected graphs as well as vacuum–vacuum graphs contribute. This formula is therefore equally valid for QCD.

It is useful to introduce a generating function for these probabilities,

$$F(z) \equiv \sum_{n=1}^{\infty} z^n P_n = \exp \left[ \frac{1}{g^2} \sum_r b_r (z^r - 1) \right]. \quad (18)$$

One can use this object in order to compute moments of the distribution of probabilities

$$\begin{aligned} \langle n \rangle &= (\ln F)'(z=1) = \frac{1}{g^2} \sum_r r b_r, \\ \langle n^2 \rangle - \langle n \rangle^2 &= (\ln F)''(z=1) = \frac{1}{g^2} \sum_r r^2 b_r, \end{aligned} \quad (19)$$

where each “prime” denotes a derivative with respect to  $z$ . Note that  $F(z=1) = \sum_n P_n = 1$ . This demonstrates explicitly that the exponential prefactor in Eq. (17) is essential for the theory to be unitary. Though we derived Eqs. (17) and (18) independently, we were alerted by Dremin [61] that an earlier version of the formulas in Eqs. (17) and (18) was derived by Gyulassy and Kauffmann [60] nearly 30 years ago also using general combinatoric arguments that did not rely on specific dynamical assumptions.

These combinatoric rules for computing probabilities (and moments thereof) in field theory with strong external sources can be mapped on to the AGK cutting rules derived in the context of reggeon field theory [62] by writing Eq. (17) as

$$P_n = \sum_{p=0}^n P_{n,p}^{(c)}, \quad (20)$$

where  $P_{n,p}^{(c)}$  denotes the probability of producing  $n$  particles in  $p$  cut sub-diagrams. One can ask directly what the probability of  $p$  cut sub-diagrams is by summing over  $n$  to obtain

$$\mathcal{R}_p \equiv \sum_{n=p}^{+\infty} P_{n,p}^{(c)} = \frac{1}{p!} \left( \frac{\sum_r b_r}{g^2} \right)^p e^{-\frac{1}{g^2} \sum_r b_r}. \quad (21)$$

This is a Poisson distribution, which is unsurprising in our framework, because disconnected vacuum–vacuum graphs are uncorrelated by definition. The average number of such cut diagrams is simply

$$\langle n_{\text{cut}} \rangle \equiv \sum_{p=0}^{+\infty} p \mathcal{R}_p = \frac{1}{g^2} \sum_r b_r. \quad (22)$$

An exact identification with Ref. [62] is obtained by expanding the exponential in Eq. (21) to order  $m - p$ , and defining

$$\mathcal{R}_{p,m} = \frac{1}{(m-p)!} \frac{1}{p!} \left( -\frac{\sum_r b_r}{g^2} \right)^{m-p} \left( \frac{\sum_r b_r}{g^2} \right)^p, \quad (23)$$

where  $\mathcal{R}_{p,m}$  is the probability of having  $p$  cut sub-diagrams out of  $m$  sub-diagrams (with  $m-p$  being the number of uncut diagrams). This distribution of probabilities can be checked to satisfy the relations

$$\begin{aligned} \text{if } m \geq 2, \quad & \sum_{p=1}^m p \mathcal{R}_{p,m} = 0, \\ \text{if } m \geq 3, \quad & \sum_{p=2}^m p(p-1) \mathcal{R}_{p,m} = 0, \\ \dots & \end{aligned} \quad (24)$$

This set of identities is strictly equivalent to the Eqs. (24) of Ref. [62] where  $m - p$  and  $p$  are identified as the numbers of uncut and cut reggeons respectively. The first relation means that diagrams with two or more subdiagrams cancel in the calculation of the multiplicity. These relations are therefore a straightforward consequence of the fact that the distribution of the numbers of cut subdiagrams is a Poisson distribution. They do not depend at all on whether these subdiagrams are “reggeons” or not. In the AGK approach, the first identity in Eq. (24) suggests that the average number of cut reggeons  $\langle n_{\text{cut}} \rangle$  can be computed from diagrams with one cut reggeon alone. The average multiplicity satisfies the relation

$$\langle n \rangle = \langle n_{\text{cut}} \rangle \langle n \rangle_1, \quad (25)$$

where  $\langle n \rangle_1$  is the average number of particles in one cut reggeon. Computing this last quantity of course requires a microscopic model of what a reggeon is.

Before going on, it is useful to summarize what we have learnt at this stage about field theories with strong external sources. We derived a general formula in Eq. (17) for the probability to produce  $n$  particles in terms of cut connected vacuum–vacuum diagrams, where  $b_r$  is the sum of the terms with  $r$  cuts. This formula is a purely combinatoric expression; it does not rely on the microscopic dynamics generating the  $b_r$ . Nevertheless, it tells us several things that were not obvious. Firstly, the probability distribution in Eq. (17) is not a Poisson distribution, *even at tree level*, if any  $b_r \neq 0$  for  $r > 1$ . It is often assumed that classical dynamics is Poissonian. We see here that the non-trivial correlations (symbolized by non-zero  $b_r$  terms

with  $r > 1$ ) in theories with self-interacting fields can produce significant modifications of the Poisson distribution.

Another immediate observation is that even the probability to produce one particle (Eq. (14)) is completely non-perturbative in the coupling constant  $g$  for arbitrarily small coupling. In other words,  $P_1$  cannot be expressed as an analytic expansion in powers of  $g$ . Therefore, while weak coupling techniques are certainly valid, such theories (the CGC for instance) are always non-perturbative. Interestingly, we will see shortly that a simple expansion in powers of the coupling exists for moments of the probability distribution. Finally, we saw that there was a simple mapping between the cutting rules first discussed in Ref. [62] and those for cut connected vacuum–vacuum graphs in field theories with strong sources.

In the rest of this lecture, we shall sketch the derivation of explicit expressions for the  $n$ -particle probabilities and for the first moment of the multiplicity distribution. Specifically, we will outline an algorithm to compute the average multiplicity up to next-to-leading order in the coupling constant. The probability for producing  $n$  particles is given by the expression

$$P_n = \frac{1}{n!} \int \left[ \prod_{i=1}^n \frac{d^3 \mathbf{p}_i}{(2\pi)^3 2E_i} \right] |\langle \mathbf{p}_1 \cdots \mathbf{p}_{n\text{out}} | 0_{\text{in}} \rangle|^2, \quad (26)$$

where  $E_i \equiv \sqrt{\mathbf{p}_i^2 + m^2}$ . The well known Lehman–Symanzik–Zimmerman (LSZ) reduction formula [63] relates the transition amplitude for producing  $n$  particles from the vacuum to the residue of the multiple poles of Green's functions of the interacting theory. It can be expressed as

$$\langle \mathbf{p}_1 \cdots \mathbf{p}_{n\text{out}} | 0_{\text{in}} \rangle = \frac{1}{Z^{n/2}} \int \left[ \prod_{i=1}^n d^4 x_i e^{ip_i x_i} (\square_{x_i} + m^2) \frac{\delta}{i\delta\rho(x_i)} \right] e^{i\mathcal{V}[\rho]}, \quad (27)$$

where the factors of  $Z$  correspond to self-energy corrections<sup>6</sup> on the cut propagators of the vacuum–vacuum diagrams. Substituting the r.h.s. of this equation into Eq. (26), and noting that

$$G_{+-}^0(x, y) = \int \frac{d^3 \mathbf{p}}{(2\pi)^3 2E_i} e^{ip(x-y)}, \quad (28)$$

is the Fourier transform of the propagator given in Eq. (12), we can write the probability  $P_n$  directly as

$$P_n = \frac{1}{n!} \mathcal{D}^n[\rho_+, \rho_-] e^{i\mathcal{V}[\rho_+]} e^{-i\mathcal{V}^*[\rho_-]} \Big|_{\rho_+ = \rho_- = \rho}, \quad (29)$$

---

<sup>6</sup> More precisely, they are the wavefunction renormalization factors.

where  $\mathcal{D}[\rho_+, \rho_-]$  is the operator

$$\mathcal{D} \equiv \int d^4x d^4y Z G_{+-}^0(x, y) \frac{\square_x + m^2}{Z} \frac{\square_y + m^2}{Z} \frac{\delta}{\delta \rho_+(x)} \frac{\delta}{\delta \rho_-(y)}. \quad (30)$$

The sources in the amplitude and the complex conjugate amplitude are labeled as  $\rho_+$  and  $\rho_-$  respectively to ensure that the functional derivatives act only on one of the two factors.

A useful and interesting identity is

$$e^{\mathcal{D}[\rho_+, \rho_-]} e^{i\mathcal{V}[\rho_+]} e^{-i\mathcal{V}^*[\rho_-]} = e^{i\mathcal{V}_{SK}[\rho_+, \rho_-]}, \quad (31)$$

where  $i\mathcal{V}_{SK}[\rho_+, \rho_-]$  is the sum of all connected vacuum–vacuum diagrams in the Schwinger–Keldysh formalism [64, 65], with the source  $\rho_+$  on the upper branch of the contour and likewise,  $\rho_-$  on the lower branch. When  $\rho_+ = \rho_- = \rho$ , it is well known that this sum of all such connected vacuum–vacuum diagrams is zero. The generating function  $F(z)$ , from Eqs. (18) and (29) is simply

$$F(z) = e^{zD} e^{i\mathcal{V}[\rho_+]} e^{-i\mathcal{V}^*[\rho_-]} \Big|_{\rho_+ = \rho_- = \rho}. \quad (32)$$

From the expression for the operator  $D$  in Eq. (30), it is clear that  $F(z)$  can be formally obtained by substituting the off-diagonal propagators  $G_{\mp, \pm}^0 \rightarrow z G_{\mp, \pm}^0$  in the usual cut vacuum–vacuum diagrams.

We shall now proceed to discuss how one computes the average multiplicity ( $F'(z = 1)$ ) of produced particles. From Eqs. (32) and (30), we obtain

$$\langle n \rangle = \int d^4x d^4y Z G_{+-}^0(x, y) \left[ \Gamma^{(+)}(x) \Gamma^{(-)}(y) + \Gamma^{(+-)}(x, y) \right]_{\rho_+ = \rho_- = \rho}, \quad (33)$$

where  $\Gamma^{(\pm)}$  and  $\Gamma^{(+-)}$  are the 1- and 2-point amputated Green's functions in the Schwinger–Keldysh formalism:

$$\begin{aligned} \Gamma^{(\pm)}(x) &\equiv \frac{\square_x + m^2}{Z} \frac{\delta i\mathcal{V}_{SK}[\rho_+, \rho_-]}{\delta \rho_{\pm}(x)}, \\ \Gamma^{(+-)}(x, y) &\equiv \frac{\square_x + m^2}{Z} \frac{\square_y + m^2}{Z} \frac{\delta^2 i\mathcal{V}_{SK}[\rho_+, \rho_-]}{\delta \rho_+(x) \delta \rho_-(y)}. \end{aligned} \quad (34)$$

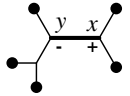
Diagrammatically,  $\langle n \rangle$  can be represented as

$$\langle n \rangle = \text{Diagram 1} + \text{Diagram 2} \quad (35)$$

Diagram 1: Two gray circles connected by a horizontal line. The left circle has a '-' sign above it, and the right circle has a '+' sign below it.  
Diagram 2: A gray circle with a '-' sign above it, connected to a white circle with a '+' sign below it by a horizontal line.

Unlike the probabilities, there is a well defined power counting for the moments of the multiplicity distribution. This is simply because the overall “absorption factor”  $\exp(-\sum_r b_r/g^2)$  present in the computation each probability, cancels when one computes averaged quantities. This is a crucial simplification, because it means that the moments of the distribution have a sensible<sup>7</sup> perturbative expansion as a series in powers of  $g^2$ .

At leading order in the coupling constant,  $\mathcal{O}(g^{-2}(g\rho)^n)$ , only the left diagram in Eq. (35) contributes. The right diagram, that contains the connected 2-point function, is a one loop diagram; in our power counting (see Eq. (7)) it starts at order  $\mathcal{O}(g^0(g\rho)^n)$ . The lowest order, where we need only tree level diagrams, can therefore be expressed as

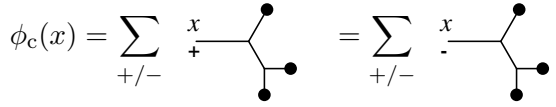
$$\langle n \rangle_{\text{LO}} = \sum_{+/-} \text{diagram} , \quad (36)$$


where the sum is over all the tree diagrams on the left and on the right of the propagator  $G_{+-}^0$  (represented in boldface) as well as a sum over the labels  $+/-$  of the vertices whose type is not written explicitly. At this order, the mass in  $G_{+-}^0$  is simply the bare mass, and  $Z = 1$ .

The diagrams in Eq. (36) can be computed using the Cutkosky rules we discussed previously. Beginning with one of the “leaves” of the tree (attached to the rest of the diagram by a  $+$  vertex for instance), one has two contributions  $G_{++}^0$  and  $-G_{+-}^0$  for the propagators connecting it to the vertex just below. (The source can be factored out, because we set  $\rho_+ = \rho_- = \rho$ .) This difference in the propagators gives

$$G_{++}^0 - G_{+-}^0 = G_{\text{R}}^0 , \quad (37)$$

where  $G_{\text{R}}^0$  is the free *retarded propagator*. (Likewise,  $G_{-+}^0 - G_{--}^0 = G_{\text{R}}^0$ .) Repeating this procedure recursively, propagators from all the “leaves” down to the root are converted into retarded propagators. It is well known that the retarded solution  $\phi_c(x)$  of the classical equations of motion with the initial conditions  $\lim_{x^0 \rightarrow -\infty} \phi_c(x) = 0$  and  $\lim_{x^0 \rightarrow -\infty} \partial^0 \phi_c(x) = 0$  can be expressed as a sum of tree diagrams built with retarded propagators. The sum over all the trees on each side of the cut in Eq. (36) can therefore be identified as

$$\phi_c(x) = \sum_{+/-} \text{diagram} = \sum_{+/-} \text{diagram} . \quad (38)$$


<sup>7</sup> The usual caveats, about the convergence of such series and issues related to their Borel summability, apply here as well.

From this discussion and Eq. (33), the leading order inclusive multiplicity can be expressed as

$$\langle n \rangle_{\text{LO}} = \int \frac{d^3 \mathbf{p}}{(2\pi)^3 2E_p} \left| \int d^4 x e^{ipx} (\square + m^2) \phi_c(x) \right|^2. \quad (39)$$

Using the identity  $e^{ipx}(\partial_0^2 + E_p^2)\phi_c(x) = \partial_0(e^{ipx}[\partial_0 - iE_p]\phi_c(x))$  and the boundary conditions obeyed by the retarded classical field  $\phi_c(x)$ , one obtains

$$E_p \frac{d\langle n \rangle_{\text{LO}}}{d^3 p} = \frac{1}{16\pi^3} \left| \lim_{x^0 \rightarrow +\infty} \int d^3 x e^{ipx} [\partial_{x^0} - iE_p] \phi_c(x) \right|^2. \quad (40)$$

The corresponding formula for gluon production in heavy ion collisions in the Color Glass Condensate framework is

$$\begin{aligned} E_p \frac{d\langle n \rangle_{\text{LO}}}{d^3 p} &= \frac{1}{16\pi^3} \lim_{x^0, y^0 \rightarrow +\infty} \int d^3 x d^3 y e^{ip(x-y)} (\partial_{x^0} - iE_p)(\partial_{y^0} + iE_p) \\ &\times \sum_{\text{phys. } \lambda} \epsilon_\mu^\lambda(\mathbf{p}) \epsilon_\nu^{\star\lambda}(\mathbf{p}) A_c^\mu(x) A_c^\nu(y), \end{aligned} \quad (41)$$

where  $\epsilon_\mu^\lambda$  is the polarization vector for the produced gluon. This is precisely the expression that was computed in previous real time numerical simulations of Yang–Mills equations *for each configuration of color sources in each of the nuclei*. To compute the distribution of gluons, we need to average over the distribution over all possible color sources as specified in Eq. (1). We will discuss results from these simulations further in Lecture II.

The leading order result in Eqs. (40) and (41) is well known. We shall now discuss the computation to next-to-leading order in the coupling — to order  $\mathcal{O}(g^0(gj)^n)$ . At this order, both terms in Eq. (33) contribute to the multiplicity. The right diagram in Eq. (35) contributes with the blob evaluated at tree level,


(42)

This contribution to the inclusive multiplicity is analogous to that of quark–antiquark pair production or gluon pair production to the respective average multiplicities for these quantities. The left diagram in Eq. (35), at this order, contains 1-loop corrections to diagrams of the kind displayed in Eq. (36). A blob on one side of the cut in Eq. (35) is evaluated at the 1 loop level (corresponding to the contribution from one loop correction to the classical



field) while the other blob is evaluated at tree level (corresponding to the contribution from the classical field itself). This can be represented as


(43)

The inclusive multiplicity at NLO includes contributions from both Eqs. (42) and (43).

To evaluate the diagram in Eq. (42), one needs to compute the propagator  $G_{+-}(x, y)$  in the presence of the background field  $\phi_c$ . This can be done by solving a Lippmann–Schwinger equation for  $G_{+-}$  [51, 56, 66]. In practice, numerical solutions of this equation can be obtained only for *retarded* or *advanced* Green’s functions in the background field. It turns out that one can express  $G_{+-}$  in terms of these as

$$G_{+-} = G_R G_R^{0-1} G_{+-}^0 G_A^{0-1} G_A, \quad (44)$$

where

$$\begin{aligned} G_R &\equiv G_R^0 + G_R^0 T_R G_R^0, \\ G_A &\equiv G_A^0 + G_A^0 T_A G_A^0. \end{aligned} \quad (45)$$

Here  $G_R^0$  ( $G_A^0$ ) is the free retarded (advanced) propagator and  $T_R$  ( $T_A$ ) is the retarded (advanced) scattering  $T$ -matrix. Substituting Eq. (45) in Eq. (44) and using the resulting expression in the second term of Eq. (33), the contribution of this term to the NLO multiplicity can be expressed as

$$\langle n \rangle_{\text{NLO}}^{(1)} = \int \frac{d^3 \mathbf{p}}{(2\pi)^3 2E_p} \int \frac{d^3 \mathbf{q}}{(2\pi)^3 2E_q} |T_R(p, -q)|^2. \quad (46)$$

One can then show that [56]

$$T_R(p, -q) = \lim_{x_0 \rightarrow +\infty} \int d^3 \mathbf{x} e^{ipx} [\partial_{x_0} - iE_p] \eta_q(x), \quad (47)$$

where  $\eta_q(x)$  is a small fluctuation field about  $\phi_c(x)$  and is the *retarded* solution of the partial differential equation

$$(\square + m^2 + g\phi_c(x))\eta_q(x) = 0, \quad (48)$$

with the initial condition  $\eta_q(x) = e^{iqx}$  when  $x_0 \rightarrow -\infty$ . Note here that  $g$  has the dimension of a mass. Note also that, despite being similar, the equation for  $\eta$  is not the classical equation of motion but is instead the equation of motion of a small fluctuation. This NLO contribution to the

inclusive multiplicity can be computed by solving an initial value problem with boundary conditions set at  $x^0 \rightarrow -\infty$ .

The other contribution of order  $\mathcal{O}(g^0(gj)^n)$  to the average multiplicity is from the diagram in Eq. (43). This contribution can be written as

$$\begin{aligned} \langle n \rangle_{\text{NLO}}^{(2)} &= \int \frac{d^3 \mathbf{p}}{(2\pi)^3 2E_p} \left[ \lim_{x_0 \rightarrow +\infty} \int d^3 \mathbf{x} e^{ipx} [\partial_0 - iE_p] \phi_c(x) \right] \\ &\times \left[ \lim_{x_0 \rightarrow +\infty} \int d^3 \mathbf{x} e^{ipx} [\partial_0 - iE_p] \phi_{c,1}(x) \right]^* + \text{c.c.} \end{aligned} \quad (49)$$

The one loop contribution to the classical field

$$\phi_{c,1}(x) = \sum_{+/-} \frac{x}{+} \text{---} \begin{array}{c} \otimes \\ | \\ \otimes \end{array} \text{---} \begin{array}{c} \otimes \\ | \\ \otimes \end{array} \text{---} \bigcirc, \quad (50)$$

includes arbitrary insertions of the background field  $\phi_c(x)$ . Following the discussion before Eq. (37) of the Cutkosky rules in this case, it can be written as [56]

$$\phi_{c,1}(x) = -ig \int d^4 y G_R(x, y) G_{++}(y, y). \quad (51)$$

We have used here the identity  $G_{++}(x, x) = G_{--}(x, x)$ . In practice,  $\phi_{c,1}(x)$  can also be obtained as the *retarded* solution to the equation

$$(\square + m^2 + g\phi_c(x)) \phi_{c,1}(x) = -g G_{++}(x, x) \quad (52)$$

with an initial condition such that  $\phi_{c,1}$  and its derivatives vanish at  $x_0 = -\infty$ . The source term in this equation can be rewritten as  $G_{++}(x, x) = \frac{1}{2} G_R (G_R^0)^{-1} G_S^0 (G_A^0)^{-1} G_A$ , where  $G_S^0(p) = 2\pi\delta(p^2 - m^2)$ . After a little algebra [56], one can show that

$$G_{++}(x, x) = \frac{1}{2} \int \frac{d^4 q}{(2\pi)^4} 2\pi\delta(q^2 - m^2) \eta_q^{(+)}(x) \eta_q^{(-)}(x). \quad (53)$$

Here  $\eta_q^{(+)}(x)$  and  $\eta_q^{(-)}(x)$  are solutions of Eq. (48) with plane wave initial conditions at  $x_0 \rightarrow -\infty$  of  $\eta_q^{(+)}(x) = e^{iqx}$  and  $\eta_q^{(-)}(x) = e^{-iqx}$ , respectively. We observe that  $G_{++}(x, x)$  contains ultraviolet divergences that arise from the integration over the momentum  $q$  in Eq. (53). They can be identified with the usual 1-loop ultraviolet divergences of the  $\phi^3$  field theory in the vacuum and must be subtracted systematically in order to obtain a finite result.

To summarize, the two NLO contributions to the inclusive multiplicity, Eqs. (46) and (49) can be computed systematically as follows. One first computes the lowest order classical field  $\phi_c(x)$  by solving the classical equations of motion, as a function of time, with the retarded boundary condition  $\phi_c(x) = 0$  at  $x^0 = -\infty$ . This computation was performed previously in the CGC framework [45–50]. The small fluctuation equation of motion in Eq. (48) is then solved in the background of  $\phi_c(x)$ , also with retarded boundary conditions at  $x^0 = -\infty$  for the small fluctuation field  $\eta_q(x)$ . This is then sufficient, from Eqs. (47) and (46), to compute one contribution to the NLO multiplicity. To compute the other, solutions of the small fluctuation equations of motion can also be used, following Eq. (53), to determine  $G_{++}(x, x)$ . Subsequent to this determination, the temporal evolution of the one loop classical field can be computed by solving Eq. (52), again with retarded boundary conditions at  $x^0 = -\infty$ . Finally, this result can be substituted in Eq. (49) in order to compute the second contribution to the NLO multiplicity.

Albeit involved and technically challenging, the algorithm we have outlined is straightforward. The extension to the QCD case can be done. Indeed, this computation is similar to a numerical computation (performed by Gelis, Kajantie and Lappi [51]) of the number of produced quark pairs in the classical background field of two nuclei.

An interesting question we shall briefly consider now is whether we can directly compute the generating function itself to some order in the coupling; even a leading order computation would contain a large amount of information. From Eqs. (32) and (30), we obtain<sup>8</sup>

$$\frac{F'(z)}{F(z)} = \int d^4x d^4y ZG_{+-}^0(x, y) \left[ \Gamma^{(+)}(z|x) \Gamma^{(-)}(z|y) + \Gamma^{(+-)}(z|x, y) \right], \quad (54)$$

where  $\Gamma^{(\pm)}(z|x)$  and  $\Gamma^{(+-)}(z|x, y)$  are defined as in Eq. (34), but must be evaluated with the substitution  $G_{\mp, \pm}^0 \rightarrow z G_{\mp, \pm}^0$  of the off-diagonal propagators. Unsurprisingly, this equation involves the same topologies as that for the average multiplicity in Eq. (35). If we can compute the expression in Eq. (54) even to leading order, the generating function can be determined directly by integration over  $z$ , since we know that  $F(1) = 1$ .

At leading order, as we have seen, only the first term in Eq. (54) contributes and (using the same trick as in Eq. (40)) Eq. (54) can be written

---

<sup>8</sup> From this relation, we see that the logarithm of  $F(z)$  has a well defined perturbative expansion in powers of  $g^2$  (that starts at the order  $g^{-2}$ ), while this is not the case for  $F(z)$  itself.



depend on time. However, assuming that both the source  $\rho(x)$  and the coupling constant  $g$  are switched off adiabatically at large negative and positive times, the coefficient functions  $f_{\pm}^{(\pm)}(z|x^0, \mathbf{p})$  become constants in the limit of infinite time ( $x^0 \rightarrow \pm\infty$ ).

The technique we use for determining the boundary conditions for the coefficients  $f_{\pm}^{(\pm)}(z|x^0, \mathbf{p})$  is reminiscent of the derivation of Green's theorem in electrostatics. We will not go into the derivation here (see Ref. [57] for the detailed derivation). The boundary conditions at  $x^0 = \pm\infty$  are

$$\begin{aligned} f_+^{(+)}(z|x^0 = -\infty, \mathbf{p}) &= 0, \\ f_-^{(-)}(z|x^0 = -\infty, \mathbf{p}) &= 0, \\ f_-^{(+)}(z|x^0 = +\infty, \mathbf{p}) &= z f_+^{(+)}(z|x^0 = +\infty, \mathbf{p}), \\ f_+^{(-)}(z|x^0 = +\infty, \mathbf{p}) &= z f_-^{(-)}(z|x^0 = +\infty, \mathbf{p}). \end{aligned} \quad (59)$$

Using Eqs. (58) and (59), we can write Eq. (55) as

$$\left. \frac{F'(z)}{F(z)} \right|_{\text{LO}} = \int \frac{d^3\mathbf{p}}{(2\pi)^3 2E_{\mathbf{p}}} f_+^{(+)}(z|+\infty, \mathbf{p}) f_-^{(-)}(z|+\infty, \mathbf{p}). \quad (60)$$

Therefore evaluating the generating function at leading order requires that we know the coefficient functions at  $x^0 = +\infty$ .

Unlike the case of partial differential equations with retarded boundary conditions, there are no straightforward algorithms for finding the solution with the boundary conditions listed in Eq. (59). Methods for solving these sorts of problems are known as “relaxation processes”. A fictitious “relaxation time” variable  $\xi$  is introduced and the simulation is begun at  $\xi = 0$  with functions  $\Phi_{\pm}$  that satisfy all the boundary conditions but not the equation of motion. These fields evolve in  $\xi$  with the equation (preserving the boundary conditions for each  $\xi$ )

$$\partial_{\xi} \Phi_{\pm} = (\square_x + m^2) \Phi_{\pm} + \frac{g}{2} \Phi_{\pm}^2 - j(x), \quad (61)$$

which admits solutions of the EOM as fixed points. The r.h.s. can in principle be replaced by any function that vanishes when  $\Phi_{\pm}$  is a solution of the classical EOM. This function should be chosen to ensure that the fixed point is attractive. A similar algorithm has been developed recently to study the real time non-equilibrium properties of quantum fields [67].

Higher moments of the multiplicity distribution can also be computed following the techniques described here. Interestingly, the variance (at leading order) can be computed once one obtains the solutions of the small fluctuation equations of motion. The computation is outlined in Ref. [57]. Thus

both the leading order variance and the NLO inclusive multiplicity can be determined simultaneously. The variance contains useful information that can convey information about the earliest stages of a heavy ion collision. In particular, correlations between particles in a range of rapidity windows can provide insight into the early stages of a heavy ion collision [68]. This provides a segue for the topic of the second lecture on the properties of the Glasma.

### 3. Lecture II: What does the Glasma look like and how does it thermalize to form a Quark Gluon Plasma?

In the previous lecture, we outlined a formalism to compute particle production in field theories with strong time dependent sources. As argued previously, the Color Glass Condensate is an example of such a field theory. In the CGC framework, the high energy factorization suggested by Eq. (1) is assumed to compute final states. In this lecture, we will address the question of how one computes in practice the initial Glasma fields after a heavy ion collision, what the properties of these fields are and outline theoretical approaches to understanding how these fields may thermalize to form a Quark Gluon Plasma. A cartoon depicting the various stages of the spacetime evolution of matter in a heavy ion collision is shown in Fig. 3.

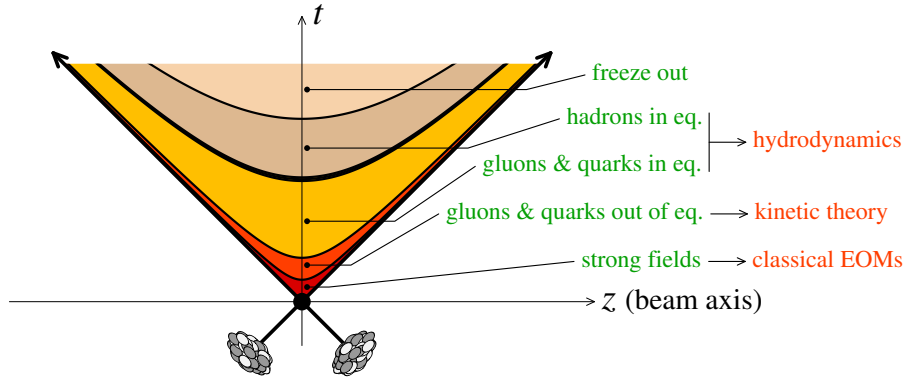


Fig. 3. Space-time development of a nucleus–nucleus collision. A goal of the Color Glass Condensate approach is to describe the first stage — dominated by strong fields — and to match it to the subsequent descriptions by kinetic theory or hydrodynamics.

In the CGC effective field theory, hard (large  $x$ ) parton modes in each of the nuclei are Lorentz contracted, static sources of color charge for the soft (small  $x$ ) wee parton, Weizsäcker–Williams modes in the nuclei. Here  $x$  is the longitudinal momentum fraction of partons in the colliding nuclei.

Wee modes with  $x \ll A^{-1/3}$  and  $k_\perp \geq \Lambda_{\text{QCD}}$  are coherent across the longitudinal extent of the nucleus and therefore couple to a large density of color sources. With increasing energy, the scale separating soft and hard modes shifts towards smaller values of  $x$ ; how this happens can be quantified by a Wilsonian RG [37]. In a heavy ion collision, the color current corresponding to the large  $x$  modes can be expressed as

$$J^{\mu,a} = \delta^{\mu+} \rho_1^a(\mathbf{x}_\perp) \delta(x^-) + \delta^{\mu-} \rho_2^a(\mathbf{x}_\perp) \delta(x^+), \quad (62)$$

where the color charge densities  $\rho_{1,2}^a$  of the two nuclei are independent sources of color charge on the light cone. Let us recall that  $x^\pm = (t \pm z)/\sqrt{2}$ . The  $\delta$  functions represent the fact that Lorentz contraction has squeezed the nuclei to infinitesimally thin sheets. The absence of a longitudinal size scale ensures that the gauge fields generated by these currents will be boost-invariant — they are independent of the space time rapidity  $\eta \equiv \text{atanh}(z/t)$ .

The gauge fields before the collision are obtained by solving the Yang–Mills equations

$$D_\mu F^{\mu\nu} = J^\nu,$$

where  $D_\mu \equiv \partial_\mu + ig[A_\mu, \cdot]$  and  $F_{\mu\nu} \equiv \partial_\mu A_\nu - \partial_\nu A_\mu + ig[A_\mu, A_\nu]$  are the gauge covariant derivative and field strength tensor, respectively, in the fundamental representation and  $[A_\mu, \cdot]$  denotes a commutator.

Before the nuclei collide ( $x^0 < 0$ ), a solution of the equations of motion is [19, 20]

$$A^\pm = 0, \quad A^i = \theta_\epsilon(x^-) \theta_\epsilon(-x^+) \alpha_1^i(\mathbf{x}_\perp) + \theta_\epsilon(x^+) \theta_\epsilon(-x^-) \alpha_2^i(\mathbf{x}_\perp), \quad (63)$$

where, here and in the following, the transverse coordinates  $x, y$  are labeled by the Latin index  $i = 1, 2$ . The subscript  $\epsilon$  on the  $\theta$ -functions denote that they are smeared by an amount  $\epsilon$  in the respective  $x^\pm$  light cone directions. We require that the functions  $\alpha_m^i(\mathbf{x}_\perp)$  ( $m = 1, 2$  denote the labels of the colliding nuclei) are such that  $F^{ij} = 0$  — they are pure gauge solutions of the equations of motion. The gauge fields, just as the Weizsäcker–Williams fields in QED, are therefore plane polarized sheets of radiation before the collision. The functions  $\alpha_m^i$  satisfy

$$-D_i \alpha_m^i = \rho_m(\mathbf{x}_\perp). \quad (64)$$

This equation has an analytical solution given by [22, 25]

$$\alpha_m^i = -\frac{i}{g} e^{iA_m} \partial^i e^{-iA_m}, \quad \nabla_\perp^2 A_m = -g \rho_m. \quad (65)$$

To obtain this result one has to assume path ordering in  $x^\pm$  respectively for nucleus 1 and 2; we assume that the limit  $\epsilon \rightarrow 0$  is taken at the end of the calculation.

We now introduce the proper time  $\tau \equiv \sqrt{t^2 - z^2} = \sqrt{2x^+x^-}$  — the initial conditions for the evolution of the gauge field in the collision are formulated on the proper time surface  $\tau = 0$ . They are obtained [42,43] by generalizing the previous ansatz for the gauge field to

$$\begin{aligned} A^i(x^-, x^+, x^\perp) &= \theta_\epsilon(x^-)\theta_\epsilon(-x^+)\alpha_1^i(\mathbf{x}_\perp) + \theta_\epsilon(-x^-)\theta_\epsilon(x^+)\alpha_2^i(\mathbf{x}_\perp) \\ &\quad + \theta_\epsilon(x^-)\theta_\epsilon(x^+)\alpha_3^i(x^-, x^+, \mathbf{x}_\perp), \\ A^\pm &= \pm x^\pm \theta_\epsilon(x^-)\theta_\epsilon(x^+)\beta(x^-, x^+, \mathbf{x}_\perp), \end{aligned} \quad (66)$$

where we adopt the Fock–Schwinger gauge condition  $A^\tau \equiv x^+A^- + x^-A^+ = 0$ . This gauge is an interpolation between the two light cone gauges  $A^\pm = 0$  on the  $x^\pm = 0$  surfaces respectively.

The gauge fields  $\alpha_3, \beta$  in the forward light cone can be determined from the known gauge fields  $\alpha_{1,2}$  of the respective nuclei before the collision by invoking a physical “matching condition” which requires that the Yang–Mills equations  $D_\mu F^{\mu\nu} = J^\nu$  be regular at  $\tau = 0$ . The  $\delta$ -functions of the current in the Yang–Mills equations therefore have to be compensated by identical terms in spatial derivatives of the field strengths. Interestingly, it leads to the unique solution [43]

$$\begin{aligned} \alpha_3^i(x^+, x^-, \mathbf{x}_\perp) &= \alpha_1^i(\mathbf{x}_\perp) + \alpha_2^i(\mathbf{x}_\perp), \\ \beta(x^+, x^-, \mathbf{x}_\perp) &= -\frac{ig}{2} [\alpha_{i,1}(\mathbf{x}_\perp), \alpha_2^i(\mathbf{x}_\perp)]. \end{aligned} \quad (67)$$

Further, the only condition on the derivatives of the fields that would lead to regular solutions are  $\partial_\tau \beta|_{\tau=0}, \partial_\tau \alpha_3^i|_{\tau=0} = 0$ .

For the purpose of solving the Yang–Mills equations for a heavy-ion collision on a lattice, we shall work with the  $\tau, \eta$  co-ordinates and re-express the initial conditions for the fields and their derivatives in terms of the fields and their conjugate momenta in these co-ordinates. Our gauge condition is  $A^\tau = 0$ , and the initial conditions in Eq. (67) for the functions  $\alpha_3^i$  and  $\beta$  at  $\tau = 0$  can be expressed in terms of the fields

$$\begin{aligned} A_i(\tau, \mathbf{x}_\perp) &\equiv A_i(\tau, \eta, \mathbf{x}_\perp), \\ \Phi(\tau, \mathbf{x}_\perp) &\equiv x^+A^-(\tau, \eta, \mathbf{x}_\perp) - x^-A^+(\tau, \eta, \mathbf{x}_\perp), \end{aligned} \quad (68)$$

where we have made manifest the fact that these fields are boost-invariant — *i.e.* independent of  $\eta$ . This is a direct consequence of the assumption in Eq. (62) that the currents are  $\delta$ -function sources on the light cone. The light cone Hamiltonian in  $A^\tau = 0$  gauge, in this case of boost invariant fields, can be written as [46]

$$\mathcal{H} = \text{Tr} \left[ \frac{E_i^2}{\tau} + \frac{(D_i \Phi)^2}{\tau} + \tau E_\eta^2 + \tau F_{xy}^2 \right]. \quad (69)$$



Here the conjugate momenta to the fields are the chromo-electric fields

$$E_i \equiv \tau \partial_\tau A_i, \quad E_\eta \equiv \frac{1}{\tau} \partial_\tau \Phi. \quad (70)$$

Note that the contribution of the hard valence current does not appear explicitly in the  $A^\tau = 0$  Hamiltonian expressed in  $(\tau, \eta)$  co-ordinates. The dependence on the color source densities is entirely contained in the dependence of the initial conditions on the source densities. Boost invariance simplifies the problem tremendously because the QCD Hamiltonian in this case is “dimensionally reduced” to a 2 + 1-d (QCD + adjoint scalar field) Hamiltonian.

In terms of these Glasma fields and their conjugate momenta, the initial conditions in Eq. (67) at  $\tau = 0$  can be rewritten as

$$\begin{aligned} A^i(0, \mathbf{x}_\perp) &= \alpha_1^i(\mathbf{x}_\perp) + \alpha_2^i(\mathbf{x}_\perp), \\ \Phi(0, \mathbf{x}_\perp) &= 0, \\ E_i(0, \mathbf{x}_\perp) &= 0, \\ E_\eta(0, \mathbf{x}_\perp) &= i g [\alpha_1^i(\mathbf{x}_\perp), \alpha_2^i(\mathbf{x}_\perp)]. \end{aligned} \quad (71)$$

The magnetic fields being defined as  $B_k \equiv \epsilon_{k\mu\nu} F^{\mu\nu}$ , these initial conditions suggest that  $B_\eta \neq 0$  and  $B_i = 0$ . Note that the latter condition follows from the constraint on the derivatives of the gauge field that ensure regular solutions at  $\tau = 0$ . Thus one obtains the interesting results that the initial Glasma fields correspond to large initial longitudinal electric and magnetic fields ( $E_\eta, B_\eta \neq 0$ ) and zero transverse electric and magnetic fields ( $E_i, B_i = 0$ ). This is in sharp contrast to the electric and magnetic fields of the nuclei before the collision (the Weizsäcker–Williams fields) which are purely transverse! Their importance was emphasized recently by Lappi and McLerran [69] who also coined the term “Glasma” to describe the properties of these fields prior to equilibration.

An immediate consequence of these initial conditions, as noted by Kharzeev, Krasnitz and Venugopalan [70], is that non-zero Chern–Simons charge can be generated in these collisions. The dynamics of the Chern–Simons number in nuclear collisions however differs from the standard discussion in two ways. Firstly, the time translational invariance of the fields is broken by the singularity corresponding to the collision. Secondly, due to the boost invariance of the solutions, there can be no non-trivial boost invariant gauge transformations. This can be seen as follows. In Ref. [70], it was shown that the Chern–Simons charge per unit rapidity could be expressed as

$$\nu = \frac{1}{16\pi^2} \int d^2 \mathbf{x}_\perp \Phi^a B_\eta^a. \quad (72)$$

Because this density is manifestly invariant under rapidity dependent transformations, such transformations (which correspond to sphaleron transitions) cannot change the Chern–Simons charge. Thus sphaleron transitions are disallowed for boost-invariant field configurations. Eqs. (71) tell us that  $\nu(\tau = 0) = 0$ ; therefore the Chern–Simons charge generated in a given window in rapidity at a time  $\tau$  is simply, by definition,  $\nu(\tau)(\eta_{\max} - \eta_{\min})$ . Since  $\eta$ 's of either sign are equally likely, the ensemble average  $\langle \nu(\tau) \rangle$  is zero. However,  $\langle \nu(\tau)^2 \rangle$  is non zero. Its value was computed in Ref. [70]. The topological charge squared per unit rapidity generated for RHIC and LHC collisions is about 1–2 units. In contrast, estimates of the same quantity in a thermal plasma are one to two orders of magnitude larger. If boost invariance is violated (as we shall soon discuss), sphaleron transitions can go, and can potentially be large. This possibility, in a different formulation, was discussed previously by Shuryak and collaborators [71].

We shall now discuss the particle distributions that correspond to the gauge fields and their conjugate momenta in the forward light cone. From the Hamilton equations

$$\frac{\partial \mathcal{H}}{\partial E_\mu} = \partial_\tau A_\mu, \quad \frac{\partial \mathcal{H}}{\partial A_\mu} = -\partial_\tau E_\mu, \quad (73)$$

the Yang–Mills equations are

$$\begin{aligned} \partial_\tau A_i &= \frac{E_i}{\tau}, \\ \partial_\tau A_\eta &= \tau E_\eta, \\ \partial_\tau E_i &= \tau D_j F_{ji} + \tau^{-1} D_\eta F_{\eta i}, \\ \partial_\tau E_\eta &= \tau^{-1} D_j F_{j\eta}. \end{aligned} \quad (74)$$

They also satisfy the Gauss law constraint

$$D_i E_i + D_\eta E_\eta = 0. \quad (75)$$

These equations are non-linear and have to be solved numerically. A lattice discretization is convenient because it preserves gauge invariance explicitly. One can write down the analogue of the well known Kogut–Susskind Hamiltonian in this case and solve Eq. (74) numerically on a discretized spatial<sup>9</sup> lattice with the initial conditions in Eq. (71). We shall not describe the numerical procedure here but instead refer the reader to Refs. [46, 49].

---

<sup>9</sup> The proper time  $\tau$  is treated as a continuous variable, that can have increments as small as required to reach the desired accuracy in the solution of the equations of motion.

Solving Hamilton's equations, the average gluon multiplicity can be computed using precisely the formula we discussed previously in Eq. (41). The result in Eq. (41) is the average multiplicity for *a* configuration of color charge densities in each of the nuclei. It is an average in the sense of being the first moment of the multiplicity distribution. This multiplicity has to be further averaged over the distribution of sources  $W_{Y_{\text{beam}}-Y}[\rho_1]$  and  $W_{Y_{\text{beam}}+Y}[\rho_2]$ , as specified in Eq. (1). These weight functionals have to be specified at an initial scale  $Y_0$  in rapidity, and are then evolved to higher rapidities by the JIMWLK renormalization group equation [25–32]. For the purposes of computing the average multiplicity in *central* Au-Au collisions at RHIC, *i.e.* for rapidities where evolution effects *à la* JIMWLK are not yet important, the weight functionals  $W_Y[\rho]$  are Gaussian distributions specified in the MV model (discussed briefly in the introduction to these lectures):

$$W_{Y_0}[\rho_{1,2}] = \exp \left( - \int d^2 \mathbf{x}_\perp \frac{\rho_{1,2}^a \rho_{1,2}^a}{2 \Lambda_s^2} \right). \quad (76)$$

Here  $\Lambda_s^2 = g^4 \mu^2$ , where  $g^2 \mu^2$  is the color charge squared of the sources per unit area. The nuclei, for simplicity, are assumed to be identical.  $\Lambda_s^2$  is the only dimensionful scale (besides the nuclear radius  $R$ ) in the problem. It is simply related, in leading order, to the nuclear saturation scale  $Q_s$  by the expression  $\Lambda_s^2 = 2\pi Q_s^2 / N_c \ln(Q_s/2L)$ , where  $L$  is an infrared scale of order  $\Lambda_{\text{QCD}}$ . The nuclear saturation scale, performing a simple extrapolation of the HERA data on the gluon distribution of the proton to Au nuclei, is of the order  $Q_s \sim 1.2\text{--}1.4$  GeV at RHIC energies in several estimates [72, 73]. For  $L = 0.2$  GeV, this corresponds to a value  $\Lambda_s = 1.66\text{--}1.8$  GeV. Clearly, there are logarithmic uncertainties in this estimate at least of order 10%. For the rest of this lecture, we will assume the Gaussian form in Eq. (76) for the averaging over sources; modifications to account for the (very likely) significant effects of small  $x$  quantum evolution will have to be considered at LHC energies.

In order to compute gluon number distributions, we impose the transverse Coulomb gauge  $\nabla_\perp \cdot \mathbf{A}_\perp = 0$  to fix the gauge freedom completely. The result for the number distributions, averaged over the sources in Eq. (76), is computed at a time  $\tau \sim 3/\Lambda_s$  to be

$$\frac{1}{\pi R^2} \frac{dN}{d\eta d^2 \mathbf{k}_\perp} = \frac{1}{g^2} \bar{f}_n \left( \frac{k_\perp}{\Lambda_s} \right), \quad (77)$$

where  $\bar{f}_n(k_\perp/\Lambda_s)$  is a function of the form

$$\bar{f}_n = \begin{cases} a_1 \left[ \exp \left( \frac{\sqrt{k_\perp^2 + m^2}}{T_{\text{eff}}} \right) - 1 \right]^{-1} & \left( \frac{k_\perp}{\Lambda_s} \leq 1.5 \right) \\ a_2 \Lambda_s^4 \ln \left( \frac{4\pi k_\perp}{\Lambda_s} \right) k_\perp^{-4} & \left( \frac{k_\perp}{\Lambda_s} > 1.5 \right) \end{cases}, \quad (78)$$

with  $a_1 = 0.137$ ,  $m = 0.0358 \Lambda_s$ ,  $T_{\text{eff}} = 0.465 \Lambda_s$ , and  $a_2 = 0.0087$ . These results are plotted in Fig. 4 — they are compared to those computed independently by Lappi [50]. The different lines in the figure correspond to different lattice discretizations; the differences at large  $k_\perp$  therefore indicate the onset of lattice artifacts, which can be eliminated by going closer to the continuum limit (larger lattices).

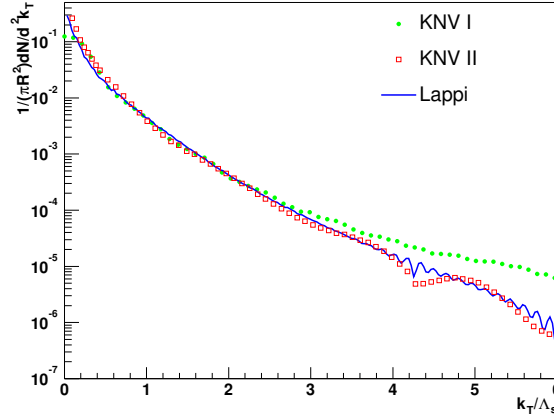


Fig. 4. Comparison of gluon transverse momentum distributions per unit area as a function of  $k_T/\Lambda_s$ . KNV I (circles): the number defined with  $k_T$  taken to mean the lattice wave number along one of the principal directions. KNV II (squares) and Lappi (solid line): the number defined by averaging over the entire Brillouin zone and with  $k_T$  taken to mean the frequency  $\omega(k_\perp)$ .

From Eq. (78), the number distribution at large  $k_\perp$  has the power law dependence one expects in perturbative QCD at leading order. For small  $k_\perp$ , the result is best fit by a massive 2- $d$  Bose–Einstein distribution even though one is solving classical equations of motion! There is an interesting discussion in the statistical mechanics literature that suggests that such a distribution may be generic for classical “glassy” systems far from equilibrium [74]. Another interesting observation is that the non-perturbative real time dynamics of the gauge fields generates a mass scale  $m$  which makes the number distributions infrared safe for finite times. Such a “plasmon mass”

can be extracted from the single particle dispersion relation; it behaves dynamically as a function of time precisely as a screening mass does [47, 53]. This can be seen in Fig. 5. As we shall discuss shortly, this plasmon mass can be related to the growth rate of instabilities in the Glasma.

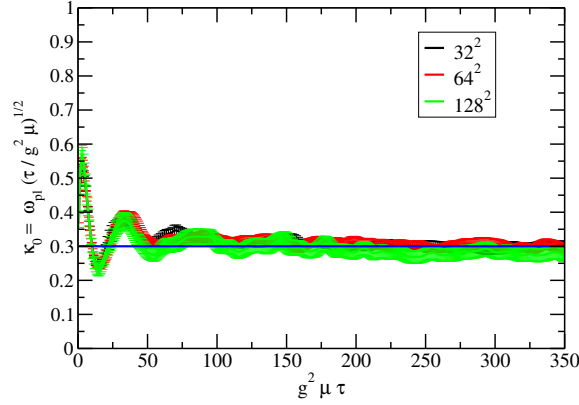


Fig. 5. Time evolution of the “plasmon frequency”  $\omega_{\text{pl}}$ , for fixed  $g^2 \mu L = 22.6$  and lattice spacings  $g^2 \mu a_\perp = 0.707, 0.354, 0.177$  ( $N_\perp = 32, 64, 128$ ), respectively.

The total transverse energy and number can be obtained independently, from the Hamiltonian density and from a gauge invariant relaxation (cooling) technique respectively. These agree with those obtained by integrating Eq. (77) over  $k_\perp$  and can be expressed as

$$\frac{1}{\pi R^2} \frac{dE_\perp}{d\eta} = \frac{f_E(\Lambda_s R)}{g^2} \Lambda_s^3, \quad \frac{1}{\pi R^2} \frac{dN}{d\eta} = \frac{f_N(\Lambda_s R)}{g^2} \Lambda_s^2, \quad (79)$$

where  $f_E = 0.27\text{--}0.25$  and  $f_N = 0.315\text{--}0.3$  for the wide range  $\Lambda_s R = 50\text{--}167$  respectively. For larger values of  $\Lambda_s R$ , the functions  $f_E$  and  $f_N$  have a weak logarithmic dependence on  $\Lambda_s R$ . If we assume parton–hadron duality and directly compare the number of gluons from Eq. (79) to the number of hadrons measured at  $\eta = 0$  in  $\sqrt{s} = 200$  GeV/nucleon Au–Au collisions at RHIC, one obtains a good agreement for  $\Lambda_s \approx 2$  GeV. This value is a little larger than the values we extracted from extrapolations of the HERA data; one should however keep in mind that additional contributions to the multiplicity of hadrons will accrue from quark and gluon production at next-to-leading order [51]. If we include these contributions, as we hope to eventually,  $\Lambda_s$  will be lower than this value.

The “formation time”  $\tau_f$ , defined as the time when the energy density  $\varepsilon$  behaves as  $1/\tau$ , is defined as  $\tau_f = 1/\gamma \Lambda_s$ , where  $\gamma = 0.3$  in the range of interest. The initial energy density for times  $\tau > \tau_f$  ( $\tau_f \approx 0.3$  fm for

$\Lambda_s = 2 \text{ GeV}$ ) is then

$$\varepsilon = \frac{1}{\tau_f} \frac{dE_\perp}{\pi R^2 d\eta} = \frac{0.26}{g^2} \frac{\Lambda_s^3}{\tau}. \quad (80)$$

This energy density, again for  $\Lambda_s = 2 \text{ GeV}$  (and  $g = 2$ ), is  $\varepsilon \approx 40 \text{ GeV/fm}^3$  at  $\tau = \tau_f$ . Because the energy density is ultraviolet sensitive, this number is probably an overestimate because the spectrum at large  $k_\perp > \Lambda_s$  in practice falls much faster than the lowest order estimate in Eq. (78). In a recent paper [75], Lappi has shown that the energy density computed in this framework, at early times has the form  $\varepsilon \sim \ln^2(1/\tau)$ ; it is finite for any  $\tau > 0$  but is not well defined strictly at  $\tau = 0$ .

In the discussion up to this point, we have assumed that the color charge squared per unit area of the source,  $g^2 \mu^2$ , is constant. However, for finite nuclei, this is not true and one can define an impact parameter dependent  $\Lambda_s$ , *i.e.*  $\Lambda_s(\mathbf{x}_\perp)$ . This generalization, in the classical Yang–Mills framework described here was discussed previously in Ref. [49] and is given by

$$\Lambda_s^2(\mathbf{x}_\perp) = \Lambda_{s0}^2 T_A(\mathbf{x}_\perp), \quad (81)$$

where  $T_A(\mathbf{x}_\perp) = \int_{-\infty}^{\infty} dz \rho_{\text{ws}}(z, \mathbf{x}_\perp)$  is the nuclear thickness profile,  $\mathbf{x}_\perp$  is the transverse coordinate vector (the reference frame here being the center of the nucleus),  $\rho_{\text{ws}}(z, \mathbf{x}_\perp)$  is the Woods–Saxon nuclear density profile, and  $\Lambda_{s0}^2$  is the color charge squared per unit area in the center of the nucleus. One can use this expression to compute the multiplicity as a function of impact parameter in the collision. Then, by using a Glauber model to relate the average impact parameter to the average number of participants [76], one can obtain the dependence of the multiplicity on the number of participants.

Previous computations of the centrality dependence of the multiplicity and of rapidity distributions were performed in the KLN approach [73, 76, 77]. There however, unlike Eq. (81), the saturation scale depends on the number of participant nucleons:

$$Q_s^2(\mathbf{x}_\perp) \sim N_{\text{part}}(\mathbf{x}_\perp), \quad (82)$$

with

$$N_{\text{part}}(\mathbf{x}_\perp) = T_A(\mathbf{x}_\perp) \left[ 1 - \left( 1 - \sigma_{NN} \frac{T_B(\mathbf{x}_\perp - \mathbf{b})}{B} \right)^B \right]. \quad (83)$$

In this formula,  $\sigma_{NN}$  is the nucleon–nucleon cross-section, and  $\mathbf{b}$  the impact parameter between the two nuclei. Note that as this form involves the thickness functions of both nuclei  $A$  and  $B$ , it is manifestly not universal — in contrast to the definition in Eq. 81. For the centrality dependence of the

multiplicity distributions, the saturation scales defined through Eqs. (81) or (82) lead to very similar results. This is because the multiplicity, at any particular  $\mathbf{x}_\perp$ , depends on the lesser of the two saturation scales, say  $Q_{s,A}$ . The dependence on the “non-universal” factor in Eq. (83) is then weak because, by definition,  $T_B$  is large.

However, the two prescriptions can be distinguished by examining a quantity of phenomenological importance, the eccentricity  $\epsilon$  defined as

$$\epsilon \equiv \frac{\int d^2\mathbf{x}_\perp \varepsilon(\mathbf{x}_\perp) (y^2 - x^2)}{\int d^2\mathbf{x}_\perp \varepsilon(\mathbf{x}_\perp) (y^2 + x^2)}. \quad (84)$$

This quantity is a measure of the asymmetry of the overlap region between the two nuclei in collisions at non zero impact parameter. In an ideal hydrodynamical description of heavy ion collisions, a larger initial eccentricity may lead to larger elliptic flow [78] than observed, thereby necessitating significant viscous effects. Comparisons of model predictions, with different initial eccentricities, to data may therefore help to constrain the viscosity of the Quark Gluon Plasma. In Fig. 6, we show results for the eccentricity from the  $k_\perp$  factorized KLN approach with the saturation scale defined as in Eq. (82) compared to the classical Yang–Mills (CYM) result computed with the definition in Eq. (81). The KLN  $N_{\text{part}}$  definition of  $Q_s$  leads to the largest eccentricity. The universal CYM definition gives smaller values of  $\epsilon$  albeit larger than the traditional parameterization (used in hydrodynamical model computations) where the energy density is taken to be proportional

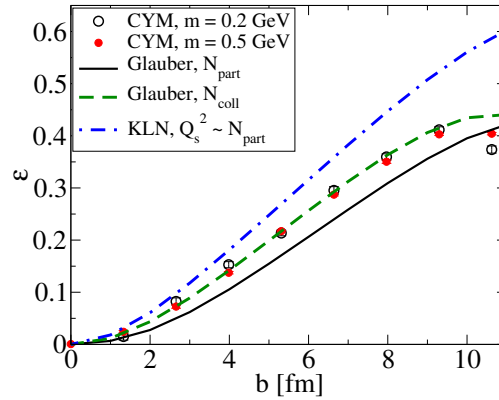


Fig. 6. The eccentricity as a function of impact parameter. The classical field CGC result with two different infrared cutoffs  $m$  is denoted by CYM [79]. The traditional initial eccentricity used in hydrodynamics is a linear combination of mostly “Glauber  $N_{\text{part}}$ ” and a small amount of “Glauber  $N_{\text{coll}}$ ”. The “KLN” curve is the eccentricity obtained from the CGC calculation in Refs. [80, 81].

to the number of participating nucleons. This result is also shown to be insensitive to two different choices of the infrared scale  $m$  which regulates the spatial extent of the Coulomb tails of the gluon distribution. A qualitative explanation of the differences in the eccentricity computed in the two approaches is given in Ref. [79] — we refer the reader to the discussion there. Also, a further elaboration of the discussion of Refs. [80,81] was very recently presented in Ref. [82] — the revised curves are closer to the result in Ref. [79].

Our discussion thus far of the Glasma has assumed strictly boost invariant initial conditions on the light cone, of the form specified in Eq. (71). However, this is clearly an idealization because it requires strict  $\delta$ -function sources as in Eq. (62), *and* that one completely disregards quantum fluctuations. Because the collision energy is ultra-relativistic and because quantum fluctuations are suppressed by one power of  $\alpha_s$ , this was believed to be a good approximation. In particular, it was not realized that violations of boost invariance lead to a non-Abelian version of the Weibel instability [55] well known in electromagnetic plasmas. To understand the potential ramifications of this instability for thermalization, let us first consider where the boost invariant results lead us. From Eq. (80), it is clear that the energy density is far from thermal — in which event, it would decrease as  $\tau^{-4/3}$ . The momentum distributions become increasingly anisotropic:  $\langle k_\perp \rangle \sim Q_s$  and  $\langle k_z \rangle \sim 1/\tau$ . Once the particle-like modes of the classical field ( $k_\perp > \Lambda_s$ ) begin to scatter, the occupation number of the field modes begins to decrease. How this occurs through scattering was outlined in an elegant scenario dubbed “bottom up” by Baier *et al.* [83]. At very early times, small elastic scattering of gluons with  $k_\perp \sim Q_s$  dominates and is responsible for lowering the gluon occupation number. The Debye mass  $m_D^2 \sim Q_s^2/(Q_s\tau)$  (see Fig. 5) sets the scale for these scattering, and the typical  $k_z$  is enhanced by collisions. One obtains  $k_z \sim Q_s/(Q_s\tau)^{1/3}$ . From this dependence, one can estimate that the occupation number of gluons is  $f < 1$  for  $\tau > \alpha_s^{-3/2}/Q_s$ . For proper times greater than these, the classical field description becomes less reliable. In the bottom up scenario, soft gluon radiation from  $2 \rightarrow 3$  scattering processes becomes important at  $\tau \sim \alpha_s^{-5/2}/Q_s$ . The system thermalizes shortly thereafter at  $\tau_{\text{therm}} = \alpha_s^{-13/5}/Q_s$  with a temperature  $T \sim \alpha_s^{2/5}Q_s$ . The thermalization time scale in this scenario is parametrically faster than that obtained by solving the Boltzmann equation for  $2 \rightarrow 2$  processes, which gives  $\tau_{\text{therm}} \sim \exp(\alpha_s^{-1/2})/Q_s$ , [84, 85]<sup>10</sup>.

The Debye mass scale is key to the power counting in the bottom up scenario. However, as pointed out recently [87] this power counting is af-

---

<sup>10</sup> For recent numerical studies of thermalization due to scattering, see Ref. [86].



fect<sup>11</sup> by an instability that arises from a change in sign of the Debye mass squared for anisotropic momentum distributions [89]. The instability is the non-Abelian analog of the Weibel instability [55] in electromagnetic plasmas and was discussed previously in the context of QCD plasmas by Mrowczynski [90]. One can view the instability, in the configuration space of the relevant fields, as the development of specific modes for which the effective potential is unbound from below [91]. Detailed simulations in the Hard-Loop effective theory in  $1 + 1$ -dimensions [87, 91, 92] and in  $3 + 1$ -dimensions [93, 94] have confirmed the existence of this non-Abelian Weibel instability. Particle-field simulations of the effects of the instability on thermalization have also been performed recently [95–97].

All of these simulations consider the effect of instabilities in systems at rest. However, as discussed previously, the Glasma expands into the vacuum at nearly the speed of light. Are they seen in the Glasma? No such instabilities were seen in the boost invariant  $2 + 1$ - $d$  numerical simulations. In the rest of this lecture, we will discuss the consequences of relaxing boost invariance in (now)  $3 + 1$ - $d$  numerical simulations of the Glasma fields<sup>12</sup>; as may be anticipated, non-Abelian Weibel instabilities also arise in the Glasma.

In heavy-ion collisions, the initial conditions on the light cone are never exactly boost invariant. Besides the simple kinematic effect of Lorentz contraction at high energies, one also has to take into account quantum fluctuations at high energies. For instance, as we discussed in the last lecture, we will have small quantum fluctuations at NLO, for each configuration of the color sources, which are not boost invariant. Parametrically, from the power counting discussed there, quantum fluctuations may be of order unity, compared to the leading classical fields which are of order  $1/g$ .

In the following, we will discuss two simple models of initial conditions containing rapidity dependent fluctuations. A more complete theory should specify, from first principles, the initial conditions in the boost non-invariant case. We will discuss later some recent work in that direction. The only condition we impose is that these initial conditions satisfy Gauss' law. We construct these by modifying the boost-invariant initial conditions in Eq. (71) to

$$\begin{aligned} E_i(0, \eta, \mathbf{x}_\perp) &= \delta E_i(\eta, \mathbf{x}_\perp), \\ E_\eta(0, \eta, \mathbf{x}_\perp) &= i g [\alpha_1^i, \alpha_2^i] + \delta E_\eta(\eta, \mathbf{x}_\perp), \end{aligned} \quad (85)$$

while keeping  $A_i, A_\eta$  unchanged. The rapidity dependent perturbations  $\delta E_i, \delta E_\eta$  are in principle arbitrary, except for the requirement that they

<sup>11</sup> For a modified “bottom up” scenario, we refer the reader to Ref. [88].

<sup>12</sup> This discussion of  $3 + 1$ - $d$  numerical simulations is based on work in Refs. [53, 54].

satisfy the Gauss law. For these initial conditions, it takes the form

$$D_i \delta E_i + D_\eta E_\eta = 0. \quad (86)$$

The boost invariance violating perturbations are constructed as follows.

- We first generate random configurations  $\delta \bar{E}_i(\mathbf{x}_\perp)$  with

$$\langle \delta \bar{E}_i(\mathbf{x}_\perp) \delta \bar{E}_j(\mathbf{y}_\perp) \rangle = \delta_{ij} \delta(\mathbf{x}_\perp - \mathbf{y}_\perp).$$

- Next, for our first model of rapidity perturbations, we generate a Gaussian random function  $F(\eta)$  with amplitude  $\Delta$

$$\langle F(\eta) F(\eta') \rangle = \Delta^2 \delta(\eta - \eta'). \quad (87)$$

For the second model, we also generate a Gaussian random function, but subsequently remove high-frequency components of  $F(\eta)$

$$F(\eta) \rightarrow F(\eta) = \int \frac{d\nu}{2\pi} e^{-i\nu\eta} e^{-|\nu|b} \int d\eta' e^{i\eta'\nu} F(\eta'), \quad (88)$$

where  $b$  acts as a “band filter” suppressing the high frequency modes. This model is introduced because the white noise Gaussian fluctuations of the previous model leads to identical amplitudes for all modes. As a consequence, the high momentum modes dominate bulk observables such as the pressure. The unstable modes we wish to focus on are sensitive to infrared modes at early times but their effects are obscured by the higher momentum modes from the white noise spectrum. This is particularly acute for large violations of boost invariance. Therefore, damping these high frequency modes allows us to also study the effect of instabilities for larger values of  $\Delta$ , or “large seeds” that violate boost-invariance.

- For both models, once  $F(\eta)$  is generated, we obtain for the fluctuation fields

$$\begin{aligned} \delta E_i(\eta, \mathbf{x}_\perp) &= \partial_\eta F(\eta) \delta \bar{E}_i(\mathbf{x}_\perp), \\ \delta E_\eta(\eta, \mathbf{x}_\perp) &= -F(\eta) D_i \delta \bar{E}_i(\mathbf{x}_\perp). \end{aligned} \quad (89)$$

These fluctuations, by construction, satisfy Gauss’ law. To implement rapidity fluctuations in the above manner, one requires  $\tau > 0$ . This is a consequence of the  $\tau, \eta$  coordinates<sup>13</sup> and does not have a physical origin. We therefore implement these initial conditions for  $\tau = \tau_{\text{init}}$  with

---

<sup>13</sup> This system of coordinates becomes singular when  $\tau \rightarrow 0$ , as can be seen from the fact that the Jacobian for the transformation from Cartesian coordinates vanishes in this limit.

$0 < \tau_{\text{init}} \ll Q_s^{-1}$ . Our results are only weakly dependent on the specific choice of  $\tau_{\text{init}}$ .

The primary gauge invariant observables in simulations of the classical Yang–Mills equations are the components of the energy-momentum tensor [46, 49]. We will discuss specifically

$$\begin{aligned} T^{xx} + T^{yy} &= 2 \text{Tr} [F_{xy}^2 + E_\eta^2] , \\ \tau^2 T^{\eta\eta} &= \tau^{-2} \text{Tr} [F_{\eta i}^2 + E_i^2] - \text{Tr} [F_{xy}^2 + E_\eta^2] . \end{aligned} \quad (90)$$

Note that the Hamiltonian density is  $\mathcal{H} = \tau T^{\tau\tau} \equiv \tau(T^{xx} + T^{yy} + \tau^2 T^{\eta\eta})$ . These components can be expressed as

$$\tau P_\perp = \frac{\tau}{2} (T^{xx} + T^{yy}) , \quad \tau P_L = \tau^3 T^{\eta\eta} , \quad (91)$$

which correspond to  $\tau$  times the mean transverse and longitudinal pressure, respectively.

When studying the time evolution of rapidity-fluctuations, it is useful to introduce Fourier transforms of observables with respect to the rapidity. For example,

$$\widetilde{P}_L(\tau, \nu, \mathbf{k}_\perp = 0) \equiv \int d\eta e^{i\eta\nu} \langle P_L(\tau, \eta, \mathbf{x}_\perp) \rangle_\perp , \quad (92)$$

where  $\langle \rangle_\perp$  denotes averaging over the transverse coordinates  $(x, y)$ . Apart from  $\nu = 0$ , this quantity would be strictly zero in the boost-invariant ( $\Delta = 0$ ) case, while for non-vanishing  $\Delta$  and  $\nu$ ,  $\widetilde{P}_L(\nu)$  has a maximum amplitude for some specific momentum  $\nu$ . Using a very small but finite value of  $\Delta$ , this maximum amplitude is very much smaller than the corresponding amplitude of a typical transverse momentum mode.

The physical parameters in this study are  $g^2\mu$  ( $=\Lambda_s$ ; see the discussion after Eq. (76)),  $L^2 = \pi R^2$ , where  $R$  is the nuclear radius,  $\Delta$ , the initial size of the rapidity dependent fluctuations and finally, the band filter  $b$ , which as discussed previously, we employ only for large values of  $\Delta$ . Physical results are expressed in terms of the dimensionless combinations  $g^2\mu\tau$  and  $g^2\mu L$ . For RHIC collisions of gold nuclei, one has  $g^2\mu L \approx 120$ ; for collisions of lead nuclei at LHC energies, this will be twice larger. The physical properties of the spectrum of fluctuations (specified in our simple model here by  $\Delta$  and  $b$ ) will presumably be further specified in a complete theory. For our present purposes, they will be treated as arbitrary parameters, and results presented for a large range in their values.

Briefly, the lattice parameters in this study, in dimensionless units, are (i)  $N_\perp$  and  $N_\eta$ , the number of lattice sites in the  $\mathbf{x}_\perp$  and  $\eta$  directions respectively; (ii)  $g^2\mu a_\perp$  and  $a_\eta$ , the respective lattice spacings; (iii)  $\tau_0/a_\perp$

and  $\delta\tau$ , the time at which the simulations are initiated and the stepping size respectively. The continuum limit is obtained by holding the physical combinations  $g^2\mu a_\perp N_\perp = g^2\mu L$  and  $a_\eta N_\eta = L_\eta$  fixed, while sending  $\delta\tau$ ,  $g^2\mu a_\perp$  and  $a_\eta$  to zero. For this study, we pick  $L_\eta = 1.6$  units of rapidity. The magnitude of violations of boost invariance, as represented by  $\Delta$ , is physical and deserves much study. The initial time is chosen to ensure that for  $\Delta = 0$ , we recover earlier  $2+1-d$  results; we set  $\tau_0 = 0.05 a_\perp$ . Our results are insensitive to variations that are a factor of 2 larger or smaller than this choice. For further details on the numerical procedure we refer the reader to Refs. [53, 54].

In Fig. 7, we plot the maximal value<sup>14</sup> of  $\tau^2 \tilde{T}^{\eta\eta} = \tilde{P}_L$  at each time step, as a function of  $g^2\mu\tau$ . The data are for a  $64^3$  lattice and correspond to  $g^2\mu L = 67.9$  and  $L_\eta = 1.6$ . The maximal value remains nearly constant until  $g^2\mu\tau \approx 250$ , beyond which it grows rapidly. A best fit to the functional form  $c_0 + c_1 \exp(c_2 \tau^{c_3})$  gives  $c_2 = 0.427 \pm 0.01$  for  $c_3 = 0.5$ ; the coefficients  $c_0$ ,  $c_1$  are small numbers proportional to the initial seed. It is clear from Fig. 7 that the form  $\exp(\Gamma \sqrt{g^2\mu\tau})$  is preferred to a fit with an exponential growth in  $\tau$ . This  $\exp(\Gamma \sqrt{g^2\mu\tau})$  growth of the unstable soft modes is closely related to the mass generated by the highly non-linear dynamics of soft modes in the Glasma. As we discussed previously, and showed in Fig. 5, a plasmon mass  $\omega_{\text{pl}} \equiv \omega(\mathbf{k}_\perp = 0)$ , is generated. After an initial transient behavior, it is of the form

$$\omega_{\text{pl}} = \kappa_0 g^2\mu \sqrt{\frac{1}{g^2\mu\tau}}. \quad (93)$$

with  $\kappa_0 = 0.3 \pm 0.01$  (this parameterization is robust as one approaches the continuum limit). The dependence on  $g^2\mu L$  is weak.

In the finite temperature Hard Thermal Loop (HTL) formalism for anisotropic plasmas, the maximal unstable modes of the stress-energy tensor grow as  $\exp(2\gamma\tau)$ , where the growth rate  $\gamma$  satisfies the relation  $\gamma = m_\infty/\sqrt{2}$  for maximally anisotropic particle distributions [87]. Here

$$m_\infty^2 = g^2 N_c \int \frac{d^3\mathbf{p}}{(2\pi)^3} \frac{f(\mathbf{p})}{p}, \quad (94)$$

where  $f(\mathbf{p})$  is the anisotropic single particle distribution of the hard modes. It was shown in Ref. [89] that  $m_\infty^2 = 3\omega_{\text{pl}}^2/2$  for both isotropic and anisotropic plasmas. One therefore obtains

$$2\gamma\tau = \sqrt{3} \frac{\kappa_0 g^2\mu}{\sqrt{g^2\mu\tau}} \tau = \sqrt{3} \kappa_0 \sqrt{g^2\mu\tau}. \quad (95)$$

---

<sup>14</sup> What we mean by this is further clarified by Fig. 8 and the related discussion there.

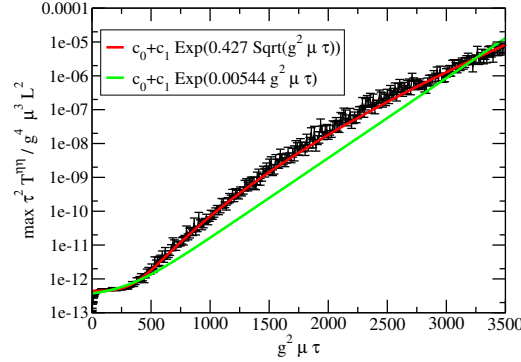


Fig. 7. The maximum Fourier mode amplitudes of the mean longitudinal pressure  $P_L = \tau^2 T^{\eta\eta}$  for  $g^2 \mu L = 67.9$ ,  $N_\perp = N_\eta = 64$ ,  $N_\eta a_\eta = 1.6$ . Also shown are best fits with  $\exp(a\tau)$  and  $\exp(a\sqrt{\tau})$  behavior. The former is clearly ruled out by the data.

For  $g^2 \mu L = 67.9$ ,  $\kappa_0 \approx 0.26$  gives the coefficient  $\sqrt{3}\kappa_0 \approx 0.447$ , which is quite close to the value obtained by a fit to the numerical data  $\Gamma_{\text{fit}} = 0.427$ . However, this agreement is misleading because a proper treatment would give in the exponent  $\int^\tau d\tau' \gamma(\tau') = \Gamma_{\text{th}} \sqrt{g^2 \mu \tau}$ , with  $\Gamma_{\text{th}} = 2\sqrt{3}\kappa_0$ . The observed growth rate is approximately half of that predicted by directly applying the HTL formalism to the Glasma. Despite obvious similarities, it is not clear that the equivalence can be expected to hold at this level of accuracy. Nevertheless, the similarities in the two frameworks is noteworthy as we will discuss now. In Fig. 8 we show the ensemble-averaged  $\tau \tilde{P}_L(\tau, \nu)$  for four different simulation times. The earliest time ( $g^2 \mu \tau \simeq 22$ ) shows the configuration before the instability sets in. At the next time, one sees a bump above the background, corresponding to the distribution of unstable modes. The unstable mode with the biggest growth rate (the cusp of the “bumps” in Fig. 8) was precisely what was used to determine the maximal growth rate  $\Gamma$  by fitting the time dependence of this mode to the form  $c_0 + c_1 \exp(\Gamma \sqrt{g^2 \mu \tau})$ . The two later time snapshots shown in Fig. 8 (for  $g^2 \mu \tau \simeq 156$  and  $g^2 \mu \tau \simeq 288$ ) indicate that the growth rate of the unstable modes closely resembles the analytic prediction from Hard-Loop calculations [87, 89].

In Fig. 8,  $\nu_{\text{max}}$  is the largest mode number that is sensitive to the instability. Its behavior is shown in Fig. 9. From this figure, one observes an underlying trend indicating a linear increase of  $\nu_{\text{max}}$  with approximately  $\nu_{\text{max}} \simeq 0.06 g^2 \mu \tau$ . For sufficiently small violations of boost-invariance, this seems to be fairly independent of the transverse or longitudinal lattice spacing we have tested. For much larger violations of boost-invariance — or sufficiently late times — one observes that  $\nu_{\text{max}}$  deviates strongly from this

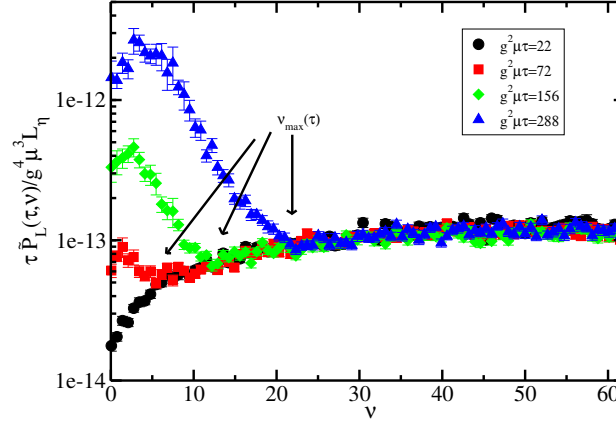


Fig. 8.  $\tau \tilde{P}_L(\tau, \nu)$  as a function of momentum  $\nu$ , averaged over 160 initial conditions on a  $16^2 \times 2048$  lattice with  $g^2 \mu L = 22.6$  and  $L_\eta = 102.4$ ,  $\Delta \simeq 10^{-11}$ . Four different simulation times show how the softest modes start growing with a distribution reminiscent of results from Hard-Loop calculations [89]. Also indicated are the respective values of  $\nu_{\max}$  for three values of  $g^2 \mu \tau$  (see text for details).

“linear law”. In Fig. 9 we show that this deviation seems to occur when the maximum amplitude of  $\tau \tilde{P}_L(\tau, \nu)$  reaches a critical size, independent of other simulation parameters. This critical value is denoted by a dashed horizontal line and has the magnitude  $3 \times 10^{-5}$  in the dimensionless units plotted there. A possible explanation for this behavior is that once the transverse magnetic field modes in the Glasma (with small  $k_\perp$ ) reach a critical size, the corresponding Lorenz force in the longitudinal direction is sufficient to bend “particle” (hard gauge mode) trajectories out of the transverse plane into the longitudinal direction. This is essentially what happens in electromagnetic plasmas. Note however that in electromagnetic plasmas the particle modes are the charged fermions. In contrast, the particle modes here are the hard ultraviolet transverse modes of the field itself. We will comment shortly on how this phenomenon may impact thermalization.

The saturation seen in Fig. 9 (bottom) is shown clearly in Fig. 10 where we plot<sup>15</sup> the temporal evolution of the maximum amplitude of the ensemble averaged  $\tau \tilde{P}_L(\tau, \nu)$ , for lattices with different  $a_\eta$ . Early times in this

<sup>15</sup> Note here that for the case of “large seed” instabilities, we consider the model with the “band filter”  $b = 0.5$ , in order to suppress the ultraviolet modes in the initial fluctuation. Note further that for larger seeds the instability systematically saturates at earlier times, as is clear from Fig. 9 (bottom).

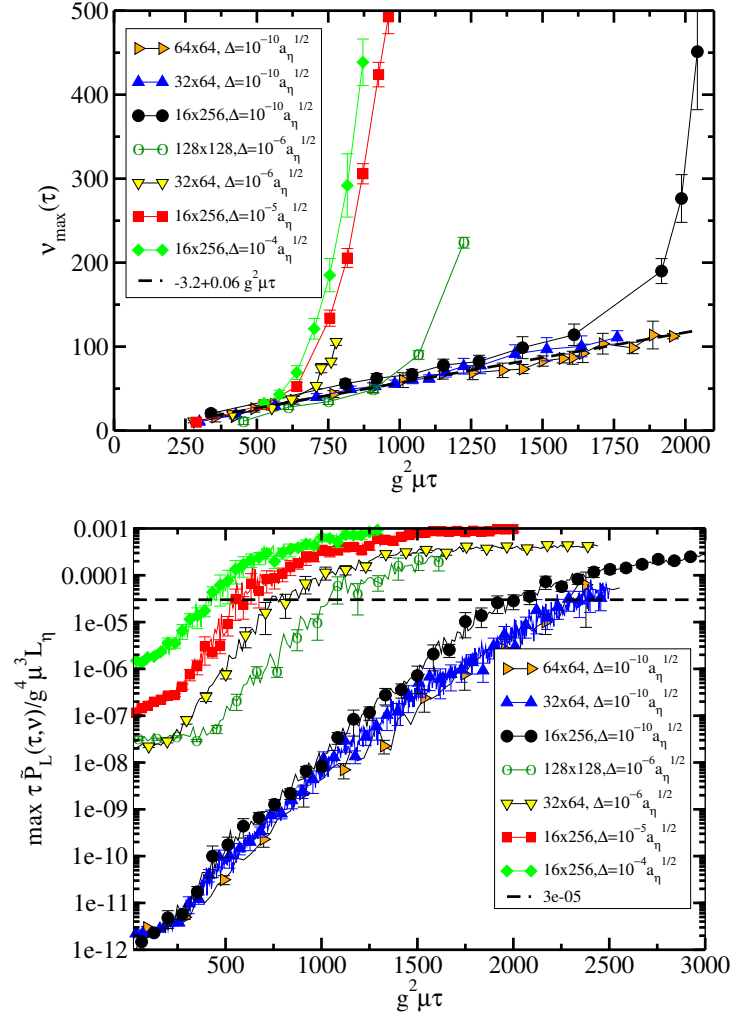


Fig. 9. Top: Time evolution of  $\nu_{\max}$ , on a lattices with  $g^2\mu L = 22.7$ ,  $L_\eta = 1.6$  and various violations of boost-invariance  $\Delta$ . The dashed line represents the linear scaling behavior. Bottom: Time evolution of the maximum amplitude  $\tau \tilde{P}_L(\tau, \nu)$ . When this amplitude reaches a certain size (denoted by the dashed horizontal line),  $\nu_{\max}$  starts to grow fast.

figure ( $g^2\mu\tau < 200$ ) correspond to the stage when the Weibel instability is operative. Interestingly, the simulations show saturation of the growth at approximately the same amplitude. These preliminary results are similar to the phenomenon of “non-Abelian saturation”, found in the context of simulations of plasma instabilities in the Hard-Loop framework [93, 94].

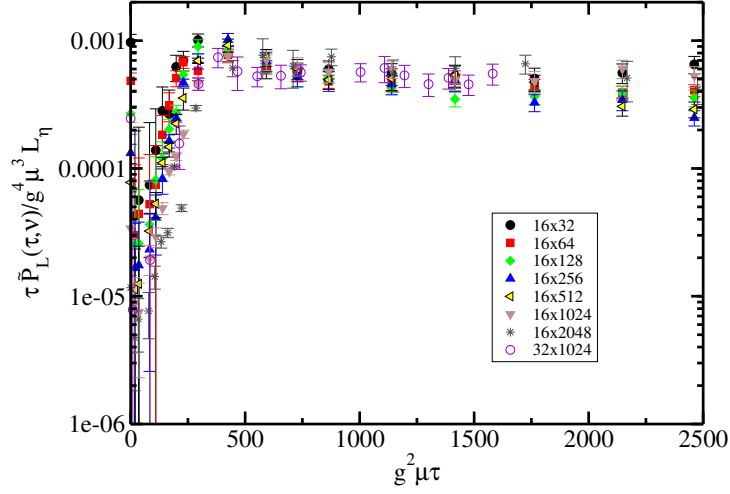


Fig.10. Time evolution of the (ensemble-averaged) maximum amplitude of  $\tau \tilde{P}_L(\tau, \nu)$ , for  $g^2 \mu L = 22.6$ ,  $L_\eta = 1.6$ ,  $N_\perp = 16, 32$ ,  $\Delta = 0.1 a_\eta^{1/2}$  and  $N_\eta$  ranging from 32 to 2048. Larger lattices correspond to smaller  $\Delta$ . This explains why the early-time behavior is not universal for the simulations shown here.

In the small seed case, the longitudinal fluctuations carry a tiny fraction of the total system energy. In the large seed case, in contrast, for the simulations shown here, the initial energy contained in the longitudinal modes is  $\sim 1\%$  of the total system energy. In reality, we expect this fraction to be significantly larger. However, this would require us to study the dynamics on even larger longitudinal lattices than those included in this study to ensure that the contributions to the pressure from ultraviolet modes are not contaminated by lattice artifacts. In Fig. 11 (top), we plot  $P_L$  as a function of  $\tau$  for different lattice spacings  $a_\eta$ . For large  $a_\eta$  (low lattice UV cutoff), the longitudinal pressure is consistent with zero; it is clearly finite when the lattice UV cutoff is raised. However, the rise saturates as there is no notable difference between the simulations for the three smallest values of the lattice spacing. At face value, this result suggests that the rise in the longitudinal pressure is physical and not a discretization artifact. Clearly, further studies on larger transverse lattices are needed to strengthen this claim.

In Fig. 11 (bottom), we investigate the time evolution of the transverse pressure and the energy density for (i) a simulation with a low UV cutoff ( $16^2 \times 32$  lattice) and (ii) a simulation with a high UV cutoff ( $16^2 \times 2048$  lattice). We observe that the rise in the mean longitudinal pressure accompanies a drop both in the mean transverse pressure and energy density. This result is consistent with the previously advocated physical mechanism of the Lorenz force bending transverse UV modes (thereby decreasing the



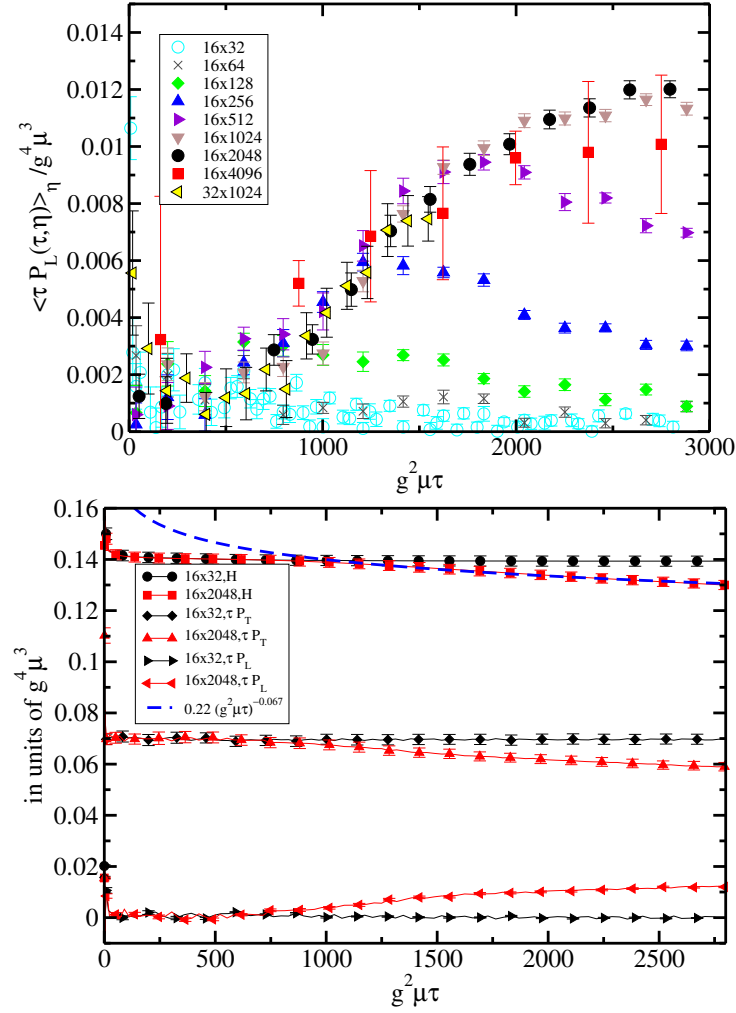


Fig.11. Top: Time evolution of the ensemble and volume averaged longitudinal pressure  $P_L$ , for lattices with  $g^2 \mu L = 22.6$ ,  $L_\eta = 1.6$ ,  $N_\perp = 16, 32$ ,  $\Delta = 0.1a_\eta^{1/2}$  and  $N_\eta$  ranging from 32 to 2048. Note : reduced statistical ensemble of 2 runs for  $N_\eta = 4096$ . Bottom: Hamiltonian density  $\langle H(\tau, \eta) \rangle_\eta$ ,  $\tau \langle P_T(\tau, \eta) \rangle_\eta$  and  $\tau \langle P_L(\tau, \eta) \rangle_\eta$ , for  $16^2 \times 32$  and  $16^2 \times 2048$  lattices. The energy density is fit to  $\varepsilon \sim \tau^{-1.067}$  at late times. All curves are calculated on lattices with  $g^2 \mu L = 22.6$ ,  $L_\eta = 1.6$  and  $\Delta = 0.1a_\eta^{1/2}$ .

transverse pressure) into longitudinal UV modes (simultaneously raising the longitudinal pressure), thereby pushing the system closer to an isotropic state. The energy density depends on the proper time as  $\varepsilon \sim \tau^{-1.067}$ , which,

while not the free streaming result of  $\varepsilon \sim \tau^{-1}$ , is also distinct from the  $\varepsilon \sim \tau^{-4/3}$  required for a locally isotropic system undergoing one dimensional expansion. Furthermore, the time scales (noting that for RHIC energies  $g^2\mu \equiv \Lambda_s \approx 2$  GeV) are much larger than the time scales of interest for early thermalization of the Glasma into a QGP. Similar results were obtained in an analytical model of the late time behavior of expanding anisotropic fields in the Hard-Loop formalism [98].

Nevertheless, these simulations are proof in principle that non-trivial dynamics can take place in the Glasma driving the system towards equilibrium. A mode analysis along the lines of that performed recently by Bökdeker and Rummukainen [99] is required to understand this dynamics in greater detail. In particular, it would be useful to understand whether the rapid shift of unstable modes to the ultraviolet (as seen in Fig. 9) is due to a turbulent Kolmogorov cascade as discussed in Refs. [100, 101]. The most important task however is to understand from first principles the spectrum of initial fluctuations that break boost invariance. A first step in this direction was taken in Ref. [102]. This issue is closely related to the NLO computation of small fluctuations outlined in Lecture I. At NLO, some of these quantum fluctuations are accompanied by large logs in  $x$ . Thus for  $\alpha_s Y \sim 1$ , these effects are large. To completely understand which contributions from the small fluctuations can be absorbed in the evolution of the initial wavefunctions<sup>16</sup>, and to isolate the remainder that contributes to the spectrum of initial fluctuations, requires that we demonstrate factorization for inclusive multiplicities. This work is in progress [103]. Finally, another interesting problem is whether one can match the temporal evolution of Glasma fields into kinetic equations at late times. Such a matching was considered previously in Ref. [104]. The early time strong field dynamics may however modify the power counting assumed in these studies — this possibility is also under active investigation [105]. In conclusion, understanding the early classical field dynamics of the Glasma and its subsequent thermalization is crucial to understand how and when the system thermalizes to form a QGP. The phenomenological implications of these studies are significant because they influence the initial conditions for hydrodynamic models. One such example that we discussed is the initial eccentricity of the QCD matter; its magnitude may be relevant for our understanding of just how “perfect”, the perfect fluid created at RHIC is.

---

<sup>16</sup> Note that the weight functionals describing the distribution of color sources, in this case, will have a dependence on rapidity described by the JIMWLK RG equations. This implies that even if the underlying classical fields are nearly boost invariant, the spectrum of gluons obtained by averaging over all color configurations, are not boost invariant. One expects significant deviations from boost invariance when rapidity varies by an amount  $\delta Y \sim 1/\alpha_s$ .

#### 4. Lecture III: Limiting fragmentation in the CGC framework

In the first two lectures, we discussed the problem of multi-particle production for hadronic collisions where the large  $x$  modes are strong sources  $\rho_{1,2} \sim 1/g$ . This is a good model of the dynamics in proton–proton collisions at extremely high energies or in heavy ion collisions already at somewhat lower energies<sup>17</sup>. In Eq. (1), one has  $\rho_{1,2}/k_\perp^2 \sim 1$ , where  $k_\perp$  is the typical momentum of the partons in the nuclei. As we then discussed in lectures I and II, there is no small parameter in the expansion in powers of these sources and one has to solve classical equations of motion numerically to compute the average inclusive multiplicities for gluon and quark production. However, for asymmetric collisions, the most extreme example of which are collisions of protons with heavy nuclei, one has a situation where  $\rho_p/k_\perp^2 \ll 1$  and  $\rho_A/k_\perp^2 \sim 1$ . The other situation where a similar power counting is applicable is when one probes forward (or backward) rapidities in proton–proton or nucleus–nucleus collisions. In these cases, one is probing large  $x$  parton distributions in one hadron (small color charge density —  $\rho_1/k_\perp^2 \ll 1$ ) and small  $x$  parton distributions in the other (large color charge density —  $\rho_2/k_\perp^2 \sim 1$ ). In these situations, analytical computations are feasible in the CGC framework. In this lecture, we will discuss the phenomenon of limiting fragmentation in this framework.

The hypothesis of limiting fragmentation [106] in high energy hadron–hadron collisions states that the pseudo-rapidity distribution  $\frac{dN}{d\eta'}$  (where  $\eta' \equiv \eta - Y_{\text{beam}}$  is the pseudo-rapidity shifted by the beam rapidity  $Y_{\text{beam}} \equiv \ln(\sqrt{s}/m_p)$ ) becomes independent of the center-of-mass energy  $\sqrt{s}$  in the region around  $\eta' \sim 0$ , *i.e.*

$$\frac{dN_{\text{ch}}}{d\eta'}(\eta', \sqrt{s}, b) = \frac{dN_{\text{ch}}}{d\eta'}(\eta', b), \quad (96)$$

where  $b$  is the impact parameter.

Limiting fragmentation appears to have a wide regime of validity. It was confirmed experimentally in  $p\bar{p}$ ,  $pA$ ,  $\pi A$  and  $AA$  collisions at high energies [107–110]. More recently, the BRAHMS and PHOBOS experiments at the Relativistic Heavy Ion Collider (RHIC) at Brookhaven National Laboratory (BNL) performed detailed studies of the pseudo-rapidity distribution of the produced charged particles  $dN_{\text{ch}}/d\eta$  for a wide range ( $-5.4 < \eta < 5.4$ ) of pseudo-rapidities, and for several center-of-mass energies ( $\sqrt{s_{\text{NN}}} = 19.6, 62.4, 130$  and  $200$  GeV) in nucleus–nucleus (Au–Au and Cu–Cu) and deuteron–nucleus ( $d$ –Au) collisions. Results for pseudo-rapidity distributions have

---

<sup>17</sup> This follows from the large density of color charges in the transverse plane of the Lorentz contracted heavy nuclei.

also been obtained over a limited kinematic range in pseudo-rapidity by the STAR experiment at RHIC [111]. These measurements have opened a new and precise window on the limiting fragmentation phenomenon.

It is worth noting that this scaling is in strong disagreement with boost invariant scenarios which predict a fixed fragmentation region and a broad central plateau extending with energy. It would therefore be desirable to understand the nature of hadronic interactions that lead to limiting fragmentation, and the deviations away from it. In a recent article, Bialas and Jeżabek [1], argued that some qualitative features of limiting fragmentation can be explained in a two-step model involving multiple gluon exchange between partons of the colliding hadrons and the subsequent radiation of hadronic clusters by the interacting hadrons. Here we will discuss how the limiting fragmentation phenomenon arises naturally within the CGC approach<sup>18</sup> — we shall address its relation to the Bialas–Jeżabek model briefly later.

Inclusive gluon production in proton–nucleus collisions was first computed in Refs. [113, 114], and shown to be  $k_\perp$  factorizable in Ref. [115]. In Ref. [116], the gluon field produced in  $p$ – $A$  collisions was computed explicitly in Lorentz gauge  $\partial_\mu A^\mu = 0$ . More recently, the gluon field was also determined explicitly in the  $A^+ = 0$  light-cone gauge [121]. The inclusive multiplicity distribution of produced gluons<sup>19</sup> can be expressed in the  $k_\perp$ -factorized form as [15, 115, 116],

$$\frac{dN_g}{dy d^2\mathbf{p}_\perp} = \frac{\alpha_s S_{AB}}{2\pi^4 C_F (\pi R_A^2)(\pi R_B^2)} \frac{1}{p_\perp^2} \int \frac{d^2\mathbf{k}_\perp}{(2\pi)^2} \phi_A(x_1, k_\perp) \phi_B(x_2, |\mathbf{p}_\perp - \mathbf{k}_\perp|). \quad (97)$$

The formula, as written here, is only valid at zero impact parameter and assumes that the nuclei have a uniform density in the transverse plane; the functions  $\phi_{A,B}$  are defined for the entire nucleus.  $S_{AB}$  denotes the transverse area of the overlap region between the two nuclei, while  $\pi R_{A,B}^2$  are the total transverse area of the nuclei, and  $C_F \equiv (N_c^2 - 1)/2N_c$  is the Casimir in the fundamental representation.

The longitudinal momentum fractions  $x_1$  and  $x_2$  are defined as

$$x_1 \equiv \frac{p_\perp}{m_p} e^{y-Y_{\text{beam}}}, \quad x_2 \equiv \frac{p_\perp}{m_p} e^{-y-Y_{\text{beam}}}, \quad (98)$$

where  $Y_{\text{beam}} = \ln(\sqrt{s}/m_p)$  is the beam rapidity,  $m_p$  is the proton mass, and  $\mathbf{p}_\perp$  is the transverse momentum of the produced gluon. The kinematics here

<sup>18</sup> Our discussion is based on our paper with Stasto [112].

<sup>19</sup> For more complicated final states, like quark–antiquark pairs,  $k_\perp$  factorization is explicitly violated [117–120].

is the  $2 \rightarrow 1$  eikonal kinematics, which provides the leading contribution to gluon production in the CGC picture.

The functions  $\phi_A$  and  $\phi_B$  are obtained from the dipole–nucleus cross-sections for nuclei  $A$  and  $B$  respectively,

$$\phi_{A,B}(x, k_\perp) \equiv \frac{\pi R_{A,B}^2 k_\perp^2}{4\alpha_s N_c} \int d^2 \mathbf{x}_\perp e^{i\mathbf{k}_\perp \cdot \mathbf{x}_\perp} \left\langle \text{Tr} \left( U^\dagger(0) U(\mathbf{x}_\perp) \right) \right\rangle_Y, \quad (99)$$

where  $Y \equiv \ln(1/x)$  and where the matrices  $U$  are adjoint Wilson lines evaluated in the classical color field created by a given partonic configuration of the nuclei  $A$  or  $B$  in the infinite momentum frame. For a nucleus moving in the  $-z$  direction, they are defined to be

$$U(\mathbf{x}_\perp) \equiv T_+ \exp \left[ -ig^2 \int_{-\infty}^{+\infty} dz^+ \frac{1}{\nabla_\perp^2} \rho(z^+, \mathbf{x}_\perp) T \right]. \quad (100)$$

Here the  $T^a$  are the generators of the adjoint representation of  $\text{SU}(N_c)$  and  $T_+$  denotes the “time ordering” along the  $z^+$  axis.  $\rho_a(z^+, \mathbf{x}_\perp)$  is a certain configuration of the density of color charges in the nucleus under consideration, and the expectation value  $\langle \cdots \rangle$  corresponds to the average over these color sources  $\rho_a$ .

As discussed previously, in the McLerran–Venugopalan (MV) model [19–21], where no quantum evolution effects are included, the  $\rho$ ’s have a Gaussian distribution, with a 2-point correlator given by

$$\langle \rho_a(0) \rho_b(\mathbf{x}_\perp) \rangle = \mu_A^2 \delta_{ab} \delta^{(2)}(\mathbf{x}_\perp - \mathbf{y}_\perp),$$

where  $\mu_A^2 \equiv A/2\pi R_A^2$  is the color charge squared per unit area. This determines  $\phi_{A,B}$  completely [115, 116], since the 2-point correlator is all we need to know for a Gaussian distribution. We will shortly discuss the small  $x$  quantum evolution of the correlator on the r.h.s. of Eq. (99).

These distributions  $\phi_{A,B}$ , albeit very similar to the canonical unintegrated gluon distributions in the hadrons, should not be confused with the latter [115, 116]. However, at large  $k_\perp$  ( $k_\perp \gg Q_s$ ), they coincide with the usual unintegrated gluon distribution. Note that the unintegrated gluon distribution here is defined such that the proton gluon distribution, to leading order satisfies

$$xG_p(x, Q^2) = \frac{1}{4\pi^3} \int_0^{Q^2} dl_\perp^2 \phi_p(x, l_\perp).$$

From Eq. (97), it is easy to see how limiting fragmentation emerges in the limit where  $x_2 \ll x_1$ . In this situation, the typical transverse momentum  $k_\perp$  in the projectile at large  $x_1$  is much smaller than the typical

transverse momentum  $|\mathbf{p}_\perp - \mathbf{k}_\perp|$  in the other projectile, because these are controlled by saturation scales evaluated respectively at  $x_1$  and at  $x_2$  respectively. Therefore, at sufficiently high energies, it is legitimate to approximate  $\phi_B(x_2, |\mathbf{p}_\perp - \mathbf{k}_\perp|)$  by  $\phi_B(x_2, p_\perp)$ . Integrating the gluon distribution over  $\mathbf{p}_\perp$ , we obtain

$$\begin{aligned} \frac{dN_g}{dy} &= \frac{\alpha_s S_{AB}}{2\pi^4 C_F (\pi R_A^2)(\pi R_B^2)} \int \frac{d^2 \mathbf{p}_\perp}{p_\perp^2} \phi_B(x_2, p_\perp) \int \frac{d^2 \mathbf{k}_\perp}{(2\pi)^2} \phi_A(x_1, k_\perp) \\ &= \frac{S_{AB}}{\pi^3 R_A^2} \int \frac{d^2 \mathbf{k}_\perp}{(2\pi)^2} \phi_A(x_1, k_\perp) \simeq \frac{S_{AB}}{\pi R_A^2} x_1 g(x_1, \mu^2 \simeq Q_s^2(x_2)). \end{aligned} \quad (101)$$

This expression is nearly independent of  $x_2$  and therefore depends only weakly on  $y - Y_{\text{beam}}$ . To obtain the second line in the above expression, we have used Eq. (99) and the fact that the Wilson line  $U$  is a unitary matrix. Therefore, details of the evolution are unimportant for limiting fragmentation, only the requirement that the evolution equation preserves unitarity. The residual dependence on  $x_2$  comes from the upper limit  $\sim Q_s^B(x_2)$  of the integral in the second line. This ensures the applicability of the approximation that led to the expression in the second line above. The integral over  $\mathbf{k}_\perp$  gives the integrated gluon distribution in the projectile, evaluated at a resolution scale of the order of the saturation scale of the target. Therefore, the residual dependence on  $y + Y_{\text{beam}}$  arises only via the scale dependence of the gluon distribution of the projectile. This residual dependence on  $y + Y_{\text{beam}}$  is very weak at large  $x_1$  because it is the regime where Bjorken scaling is observed.

The formula in Eq. (101) was used previously in Ref. [122]. The nuclear gluon distribution here is determined by global fits to deeply inelastic scattering and Drell–Yan data. We note that the glue at large  $x$  is very poorly constrained at present [123]. The approach of Bialas and Jezabek [1] also amounts to using a similar formula, although convoluted with a fragmentation function (see Eqs. (1), (4) and (5) of [1] — in addition, both the parton distribution and the fragmentation function are assumed to be scale independent in this approach). We will discuss the effect of fragmentation functions later in our discussion.

Though limiting fragmentation can be simply understood as a consequence of unitarity in the high energy limit, what may be more compelling are observed deviations from limiting fragmentation and how these vary with energy. We will now see whether deviations from limiting fragmentation can be understood from the renormalization group (RG) evolution of the unintegrated gluon distributions in Eq. 97. In particular, we study the RG evolution of these distributions given by the Balitsky–Kovchegov (BK) equation [33, 34].

The BK equation is a non-linear evolution equation<sup>20</sup> in rapidity  $Y = \ln(1/x)$  for the forward scattering amplitude  $T(r_\perp, Y)$  of a *quark-antiquark dipole* of size  $r_\perp$  scattering off a target in the limit of very high center-of-mass energy  $\sqrt{s}$  where  $T$  is defined as:

$$T(r_\perp, Y) = 1 - \frac{1}{N_c} \text{Tr} \left\langle \tilde{U}^\dagger(0) \tilde{U}(\mathbf{r}_\perp) \right\rangle_Y. \quad (102)$$

Here  $\tilde{U}$  is the corresponding Wilson line for the scattering of a quark-antiquark dipole in the *fundamental* representation. The correlators  $U$  in Eq. (99), which are in the *adjoint* representation are Wilson lines for the scattering of a gluon dipole on the same target instead. The BK equation captures essential features of high energy scattering. When  $r_\perp \ll 1/Q_s$ , one has color transparency; for  $r_\perp \gg 1/Q_s$ , the amplitude  $T \rightarrow 1$ , and one obtains gluon saturation<sup>21</sup>. It is therefore an excellent model to study both limiting fragmentation as well as deviations from it.

It is convenient to express the BK equation in momentum space in terms of the Bessel-Fourier transform of the amplitude

$$\tilde{T}(k_\perp, Y) \equiv \int_0^{+\infty} \frac{dr_\perp}{r_\perp} J_0(k_\perp r_\perp) T(r_\perp, Y). \quad (103)$$

One obtains

$$\frac{\partial \tilde{T}(k_\perp, Y)}{\partial Y} = \bar{\alpha}_s (K \otimes \tilde{T})(k_\perp, Y) - \bar{\alpha}_s \tilde{T}^2(k_\perp, Y), \quad (104)$$

where we denote  $\bar{\alpha}_s \equiv \alpha_s N_c / \pi$ . The operator  $K$  is the well known BFKL kernel in momentum space [10, 11].

In the large  $N_c$  and large  $A$  limit, the correlators of Wilson lines in the fundamental and adjoint representations are simply related:

$$\frac{1}{N_c} \text{Tr} \langle U(0) U^\dagger(\mathbf{r}_\perp) \rangle_Y = N_c [1 - T(r_\perp, Y)]^2.$$

One can therefore express the unintegrated gluon distribution in Eq. (99) in terms of  $T$  as

$$\phi_{A,B}(x, k_\perp) = \frac{\pi^2 R_A^2 N_c k_\perp^2}{2 \alpha_s} \int_0^{+\infty} r_\perp dr_\perp J_0(k_\perp r_\perp) \left[ 1 - T_{A,B} \left( r_\perp, \ln \left( \frac{1}{x} \right) \right) \right]^2. \quad (105)$$

<sup>20</sup> It is equivalent to the corresponding JIMWLK equation [25–32] of the Color Glass Condensate, in a mean field (large  $N_c$  and large  $A$ ) approximation where higher order dipole correlators are neglected.

<sup>21</sup>  $Q_s$  is defined in terms of the requirement that  $T = 1/2$  for  $r_\perp = 2/Q_s$ .

In Ref. [112] we solved the BK equation numerically, in both fixed and running coupling cases, in order to investigate limiting fragmentation in hadronic collisions<sup>22</sup>. The results are shown in Fig. 12. The solid line is the

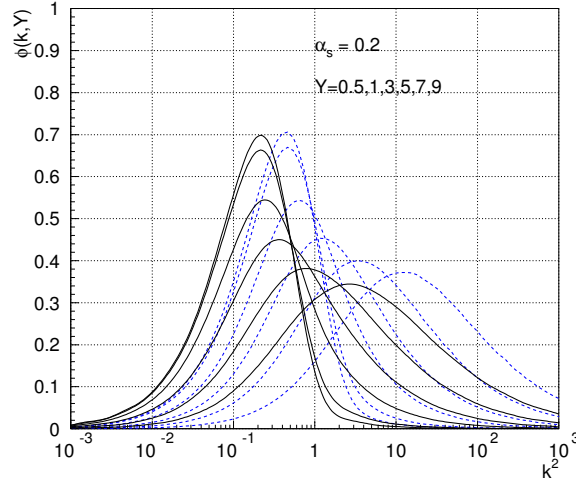


Fig.12. The unintegrated gluon distribution from (i) correlators in the adjoint representation (Eq.105) (dashed lines) and (ii) correlators in the fundamental representation — see text (solid lines).

result obtained for the unintegrated distribution corresponding to correlators in the fundamental representation, *i.e.* proportional to the Fourier transform of  $1 - T$  instead of that of  $N_c(1 - T)^2$  in Eq. (105).

Our results for limiting fragmentation are obtained through the following procedure:

- One first solves the BK equation in Eq. (104) to obtain (via Eq. (103)) Eq. (105) for the unintegrated distributions  $\phi(x, k_\perp)$ . The solution is performed for  $x \leq x_0 = 10^{-2}$  with the initial condition  $\phi(x_0, k_\perp)$ , given by the McLerran–Venugopalan model [19–21] with a fixed initial value of the saturation scale  $Q_s^A(x_0)$ . For a gold nucleus, extrapolations from HERA and estimates from fits to RHIC data suggest that  $(Q_s^A(x_0))^2 \approx 2 \text{ GeV}^2$ . The saturation scale in the proton is taken to be  $Q_s^2(x_0) = (Q_s^A(x_0))^2 (197/A)^{1/3}$ . For comparison, we also considered initial conditions from the Golec-Biernat and Wusthoff (GBW) model [129]. The values of  $Q_s^A$  were varied in this study to obtain best fits to the data.

<sup>22</sup> The BK equation was solved numerically previously for various studies [124–128].



- We used the ansatz

$$\phi(x, k_{\perp}) = \left( \frac{1-x}{1-x_0} \right)^{\beta} \left( \frac{x_0}{x} \right)^{\lambda_0} \phi(x_0, k_{\perp}),$$

in order to extrapolate our results to larger values of  $x > x_0$ , where the parameter  $\beta = 4$  is fixed by QCD counting rules.

- The resulting expressions are substituted in Eq. (97) to determine rapidity distribution of the produced gluons. The pseudo-rapidity distributions are determined by multiplying Eq. (97) with the Jacobian for the transformation from  $y$  to  $\eta$ . This transformation requires one to specify an infrared mass, which is also the mass chosen to regulate the (logarithmic) infrared sensitivity of the rapidity distributions.

For further details on how the results are obtained, we refer the reader to Ref. [112].

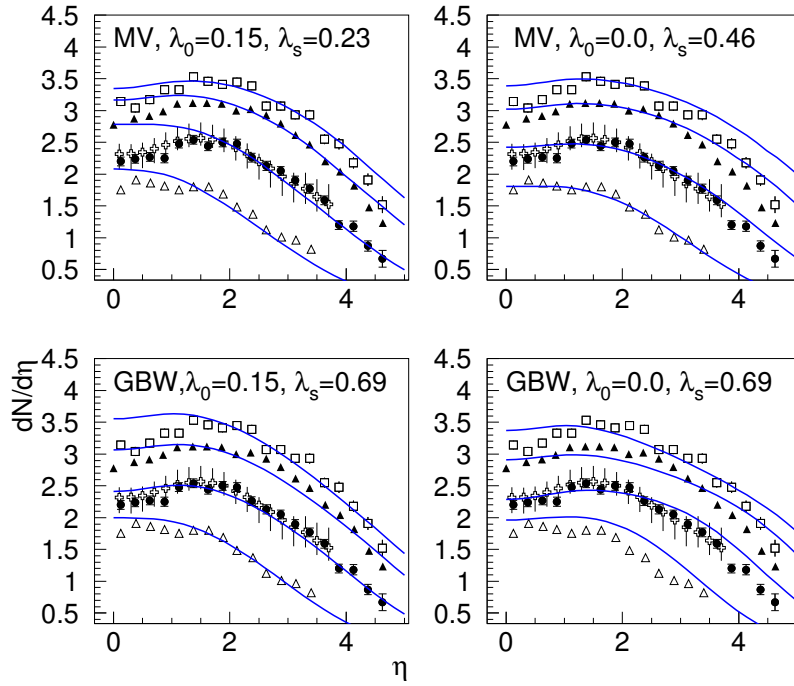


Fig. 13. Pseudorapidity distributions  $dN/d\eta$  for charged particles from nucleon-nucleon collisions at UA5 energies [107]  $\sqrt{s} = 53, 200, 546, 900$  GeV and PHOBOS data [110] at  $\sqrt{s} = 200$  GeV. Upper plots: initial distribution from the MV model, lower plots: initial distribution from the GBW model. Left panels:  $\lambda_0 = 0.15$ , right panels  $\lambda_0 = 0.0$ .

In Fig. 13, we plot the pseudo-rapidity distributions of the charged particles produced in nucleon–nucleon collisions for center of mass energies ranging from 53 GeV to 900 GeV. The computations were performed for input distributions (for BK evolution) at  $x_0 = 0.01$  from the GBW and MV models. The normalization is a free parameter which is fitted at one energy. Plots on the left of Fig. 13 are obtained for  $\lambda_0 = 0.15$  (the free parameter in the large  $x$  extrapolation) whereas the right plots are for  $\lambda_0 = 0.0$ . The different values of  $\lambda_s = 4.88\bar{\alpha}_s$  are obtained for different values of  $\alpha_s$  as inputs to the BK equation. While these values of  $\alpha_s$  might appear small, they can be motivated as follows. The amplitude has the growth rate  $\lambda_{\text{BK}} = 2.77 \lambda_s / 4.88 \approx 0.57 \lambda_s$ . Thus  $\lambda_s = 0.46$ , which gives reasonable fits (more on this in the next paragraph) to the  $pp$  data for the MV initial conditions, corresponds to  $\lambda_{\text{BK}} = 0.28$ . Thus a small value of  $\alpha_s$  in fixed coupling computations “mimics” the value for the energy dependence of the amplitude in next-to-leading order resummed BK computations [39] and in empirical dipole model comparisons to the HERA data [129].

Our computations are extremely sensitive to the extrapolation prescription to large  $x$ . This is not a surprise as the wave-function of the projectile is probed at fairly large values of  $x_1$ . From our analysis, we see that the data naively favors a non-zero value for  $\lambda_0$ . The value  $\lambda_0 = 0$  results in distributions which, in both the MV and GBW cases, give reasonable fits (albeit with different normalizations) at lower energies but systematically become harder relative to the data as the energy is increased. To fit the data in the MV model up to the highest UA5 energies, a lower value of  $\lambda_s$  than that in the GBW model is required. This is related to the fact that MV model has tails which extend to larger values in  $k_\perp$  than in the GBW model. As the energy is increased, the typical  $k_\perp \sim Q_s(x_2)$  does as well. We will return to this point shortly.

In Fig. 14 the same distributions are shown as a function of the  $\eta' = \eta - Y_{\text{beam}}$ . The calculations for  $\lambda_0 = 0.15$  are consistent with scaling in the limiting fragmentation region. There is a slight discrepancy between the calculations and the data in the mid-rapidity region. This discrepancy may be a hint that one is seeing violations of  $k_\perp$  factorization in this regime because  $k_\perp$  factorization becomes less reliable the further one is from the dilute-dense kinematics of the fragmentation regions [45, 130]. This discrepancy should grow with increasing energy. However, our parameters are not sufficiently constrained that a conclusive statement can be made. For instance, as we mentioned previously, there is a sensitivity to the infrared mass chosen in the Jacobian of the transformation from  $y$  to  $\eta$ . This is discussed further in Ref. [112].

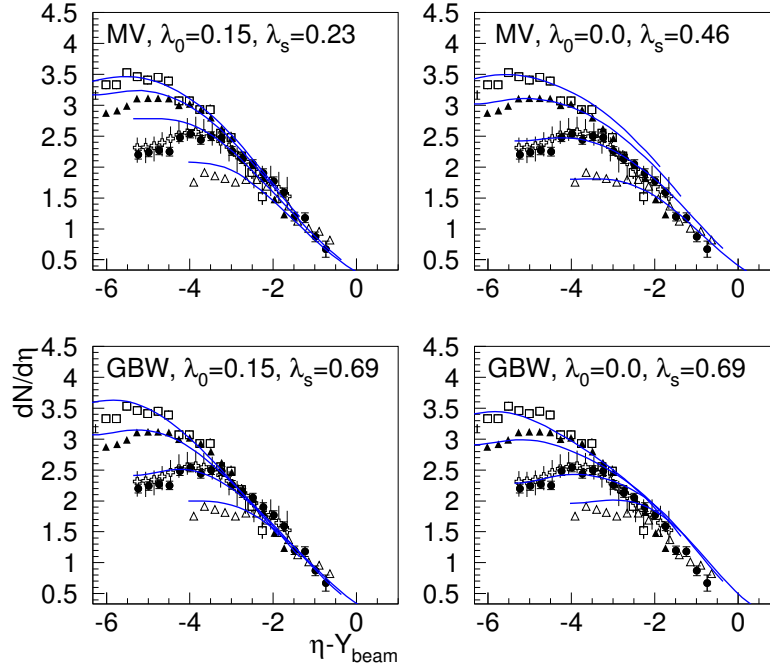


Fig. 14. The same as Fig. 13 but plotted *versus*  $\eta' = \eta - Y_{\text{beam}}$  to illustrate the region of limiting fragmentation.

In Fig. 15 we show the extrapolation to higher energies, in particular the LHC range of energies for the calculation with the GBW input. We observed previously that the MV initial distribution, when evolved to these higher energies, gives a rapidity distribution which is very flat in the range  $-5 < \eta < 5$ . We noted that this is because the average transverse momentum grows with the energy giving a significant contribution from the high  $k_{\perp}$  tail of the distribution in the MV input at  $x_0$ . The effect of fragmentation functions on softening the spectra in the limiting fragmentation region can be simply understood by the following qualitative argument. The inclusive hadron distribution can be expressed as

$$\frac{dN_h}{d^2\mathbf{p}_{\perp}dy} = \int_{z_{\min}}^1 \frac{dz}{z} \frac{dN_g}{d^2\mathbf{q}_{\perp}dy} D_{g \rightarrow h} \left( z = \frac{p_{\perp}}{q_{\perp}}, \mu^2 \right), \quad (106)$$

where  $D_{g \rightarrow h}(z, \mu^2)$  is the fragmentation function denoting the probability, at the scale  $\mu^2$ , that a gluon fragments into a hadron carrying a fraction  $z$  of its transverse momentum. For simplicity, we only consider here the probability for gluons fragmenting into the hadron. The lower limit of the

integral can be determined from the kinematic requirement that  $x_{1,2} \leq 1$  — we obtain,

$$z_{\min} = \frac{q_{\perp}}{m_p} e^{y-Y_{\text{beam}}} . \quad (107)$$

If  $z_{\min}$  were zero, the effect of including fragmentation effects would simply be to multiply Eq. (106) by an overall constant factor. At lower energies, the typical value of  $q_{\perp}$  is small for a fixed  $y - Y_{\text{beam}}$ ; the value of  $z_{\min}$  is quite low. However, as the center of mass energy is increased, the typical  $q_{\perp}$  value grows slowly with the energy. This has the effect of raising  $z_{\min}$  for a fixed  $y - Y_{\text{beam}}$ , thereby lowering the value of the multiplicity in Eq. (106) for that  $y - Y_{\text{beam}}$ . Note further that Eq. (107) suggests that there is a kinematic bound on  $q_{\perp}$  as a function of  $y - Y_{\text{beam}}$  — only very soft gluons can contribute to the inclusive multiplicity.

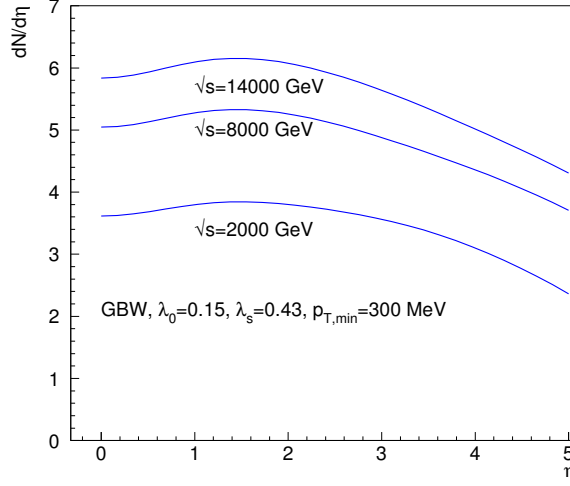


Fig. 15. Predictions for higher center-of-mass energies for proton–proton collisions:  $\sqrt{s} = 2, 8, 14$  TeV for GBW input model. The parameter in the large  $x$  extrapolation was set to  $\lambda_0 = 0.15$ .

In Fig. 16 we display the  $p_{\perp}$  distributions obtained from the MV input compare to the UA1 data [131]. We compare the calculation with and without the fragmentation function. The fragmentation function has been taken from [132]. Clearly the “bare” MV model does not describe the data at large  $k_{\perp}$  because it does not include fragmentation function effects which, as discussed, make the spectrum steeper. In contrast, because the  $k_{\perp}$  spectrum of the GBW model dies exponentially at large  $k_{\perp}$ , this “unphysical”  $k_{\perp}$  behavior mimics the effect of fragmentation functions — see Fig. 16. Hence extrapolations of this model, as shown in Fig. 18 give a more reasonable looking result. Similar conclusions were reached previously in Ref. [133].

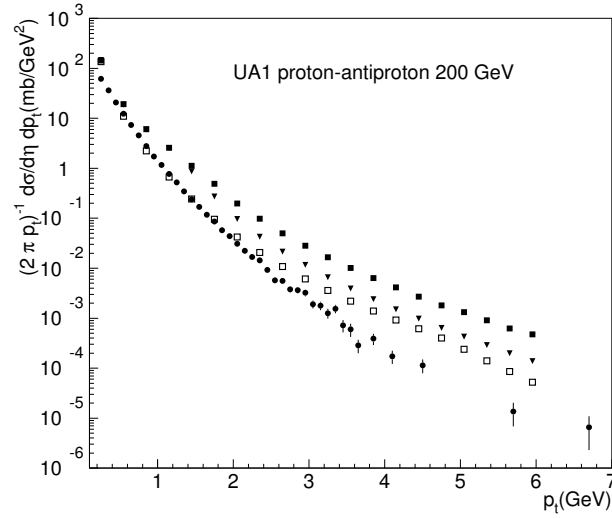


Fig. 16.  $p_{\perp}$  distribution from Eq. (97) with MV (full squares) and GBW (full triangles) initial conditions. The MV initial condition — with the fragmentation function included — is denoted by the open squares. The distribution is averaged over the rapidity region  $y = 0.0 - 2.5$ , to compare with data (in 200 GeV/nucleon proton-antiproton collisions in the same pseudo-rapidity range) on charged hadron  $p_{\perp}$  distributions from the UA1 Collaboration: full circles.

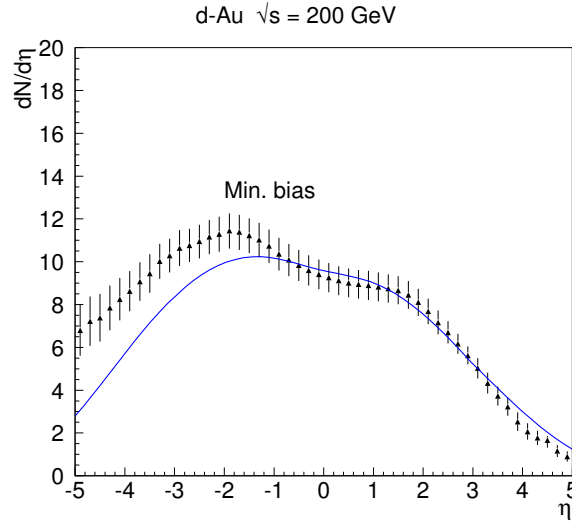


Fig. 17. Comparison of theory (with MV input) to minimum bias deuteron-gold data at RHIC [135].

We next compute the pseudo-rapidity distribution in deuteron-gold collisions. In Fig. 17 we show the result for the calculation compared with the  $d$ - $A$  data [135]. The unintegrated gluons were extracted from the  $pp$  and  $AA$  data. The overall shape of the distribution matches well on the deuteron side with the minimum-bias data. The disagreement on the nuclear fragmentation side is easy to understand since, as mentioned earlier, it requires a better implementation of nuclear geometry effects. Similar conclusions were reached in Ref. [134] in their comparisons to the RHIC deuteron-gold data.

We now turn to nucleus-nucleus collisions. In Fig. 18 we present fits to data on the pseudo-rapidity distributions in gold-gold collisions from the PHOBOS, BRAHMS and STAR Collaborations. The data [110] are for  $\sqrt{s} = 19.6, 130, 200$  GeV and the BRAHMS data [109] are for  $\sqrt{s} = 130, 200$  GeV. A reasonable description of limiting fragmentation is achieved in this case as well. One again has discrepancies in the central rapidity region as in the  $pp$  case. We find that values of  $Q_s^A \approx 1.3$  GeV for the saturation scale give the best fits. This value is consistent with the other estimates discussed previously [48, 72, 77]. Apparently the gold-gold data are better described by the calculations which have  $\lambda_0 = 0.0$ . This might be related to the difference in the large  $x$  distributions in the proton and nucleus. Further, slightly higher values of  $\lambda_s$  are preferred to the  $pp$  case. This variation of parameters from  $AA$  to  $pp$  case might be also connected with the fact that in our approach the impact parameter is integrated out thereby averaging over details of the nuclear geometry.

In Fig. 19 we show the extrapolation of two calculations to higher energy  $\sqrt{s} = 5500$  GeV. We note that the calculation within the MV model gives results which would violate the scaling in the limiting fragmentation region by approximately 20% at larger  $y - Y_{\text{beam}}$ . This violation is due partly to the effect of fragmentation functions discussed previously and partly to the fact that the integrated parton distributions from the MV model do not obey Bjorken scaling at large values of  $x$ . In the latter case, the violations are proportional to  $\ln(Q_s^2(x_2))$  as discussed previously. The effects of the former are simulated by the GBW model — the extrapolation of which, to higher energies, is shown by the dashed line. The band separating the two therefore suggests the systematic uncertainty in such an extrapolation coming from (i) the choice of initial conditions and (ii) the effects of fragmentation functions which are also uncertain at lower transverse momenta.

To summarize the discussion in this lecture, we studied the phenomenon of limiting fragmentation in the Color Glass Condensate framework. In the dilute-dense (projectile-target) kinematics of the fragmentation regions, one can derive (in this framework) an expression for inclusive gluon distributions which is  $k_\perp$  factorizable into the product of “unintegrated” gluon distributions in the projectile and target. From the general formula for

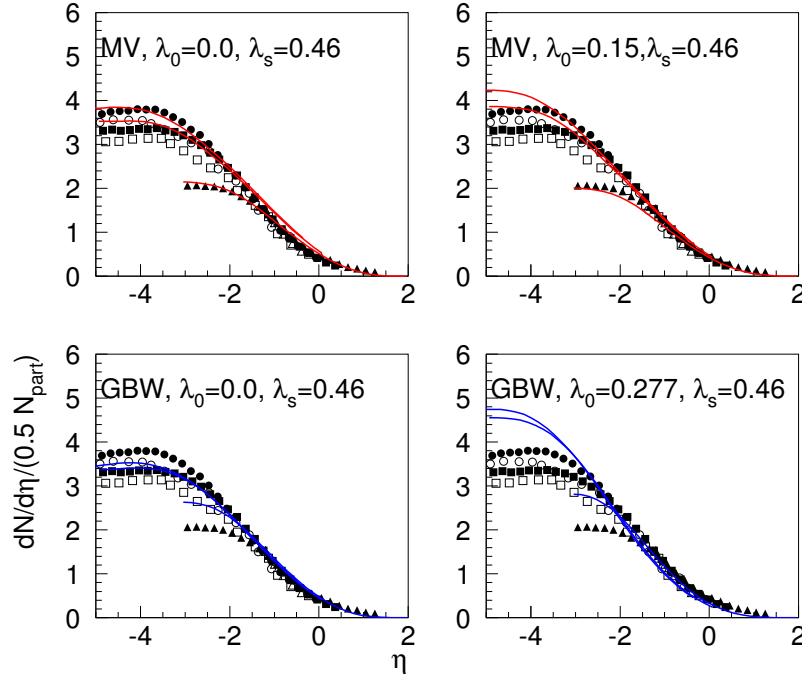


Fig. 18. Pseudorapidity distributions normalized by the number of participants for charged hadrons in gold–gold collisions from the PHOBOS Collaboration at energies 19.6, 130, 200 GeV (filled triangles, squares and circles), BRAHMS Collaboration at energies 130, 200 GeV (open squares and circles). The data from the STAR Collaboration at energy 62.4 GeV (open triangles) are not visible on this plot but can be seen more clearly in Fig. 19. Upper solid line: initial distributions from the MV model; lower solid line: initial distributions from the GBW model.

gluon production (Eq. (97)), limiting fragmentation is a consequence of two factors:

- Unitarity of the  $U$  matrices which appear in the definition of the unintegrated gluon distribution in Eq. (99).
- Bjorken scaling at large  $x_1$ , namely, the fact that the integrated gluon distribution at large  $x$ , depends only on  $x_1$  and not on the scale  $Q_s(x_2)$ . (The residual scale dependence consequently leads to the dependence on the total center-of-mass energy.)

Deviations from the limiting fragmentation curve at experimentally accessible energies are very interesting because they can potentially teach us about how parton distributions evolve at high energies. In the CGC framework, the

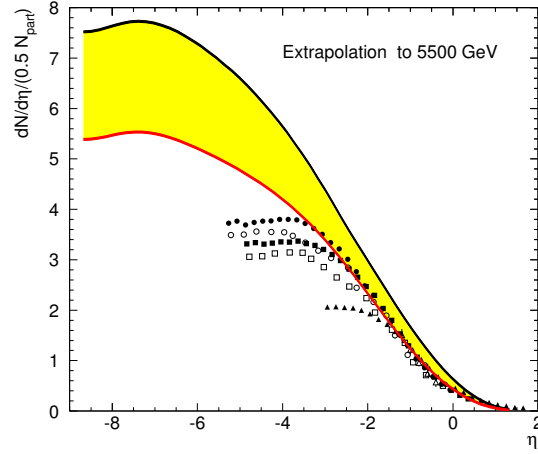


Fig. 19. Extrapolation of calculations for gold–gold collisions shown in Fig. 18 to the LHC energy  $\sqrt{s} = 5500$  GeV/ nucleon. For comparison, the same data at lower energies are shown. (See Fig. 18.) Dashed line — GBW input  $\lambda_0 = 0, \lambda_s = 0.46$ , solid line — MV input with  $\lambda_0 = 0, \lambda_s = 0.46$ .

Balitsky–Kovchegov equation determines the evolution of the unintegrated parton distributions with energy from an initial scale in  $x$  chosen here to be  $x_0 = 0.01$ . This choice of scale is inspired by model comparisons to the HERA data.

We compared our results to data on limiting fragmentation from  $pp$  collisions at various experimental facilities over a wide range of collider energies, and to collider data from RHIC for deuteron–gold and gold–gold collisions. We obtained results for two different models of initial conditions at  $x \geq x_0$ ; the model MV and the GBW model.

We found reasonable agreement for this wide range of collider data for the limited set of parameters and made predictions which can be tested in proton–proton and nucleus–nucleus collisions at the LHC. Clearly these results can be fine tuned by introducing further details about nuclear geometry. More parameters are introduced, however there is more data for different centrality cuts — we leave these detailed comparisons for future studies. In addition, an important effect, which improves agreement with data, is to account for the fragmentation of gluons in hadrons. In particular, the MV model, which has the right leading order large  $k_\perp$  behavior at the partonic level, but no fragmentation effects, is much harder than the data. The latter falls as a much higher power of  $k_\perp$ . As rapidity distributions at higher energies are more sensitive to larger  $k_\perp$ , we expect this discrepancy to show up in our studies of limiting fragmentation and indeed it does. Taking this into account leads to more plausible extrapolations of fits of existing data to LHC energies.



These lectures were delivered by one of us (R.V.) at the XLVI Zakopane School in Theoretical Physics. This school held a special significance because it coincided with the 70<sup>th</sup> birthday of Andrzej Białas who is a founding member of the school. R.V. would like to thank Michał Praszalowicz for his excellent organization of the school. This work has drawn on recent results obtained by one or both of us in collaboration with H. Fujii, K. Fukushima, S. Jeon, K. Kajantie, T. Lappi, L. McLerran, P. Romatschke and A. Stasto. We thank them all. R.V. was supported by DOE Contract No. DE-AC02-98CH10886.

## REFERENCES

- [1] A. Bialas, M. Jeżabek, *Phys. Lett.* **B590**, 233 (2004).
- [2] R. Venugopalan, *Acta Phys. Pol. B* **30**, 3731 (1999).
- [3] K. Adcox *et al.* [PHENIX Collaboration], *Nucl. Phys.* **A757**, 184 (2005);  
J. Adams *et al.* [STAR Collaboration], *Nucl. Phys.* **A757**, 102 (2005);  
B.B. Back *et al.* [PHOBOS Collaboration], *Nucl. Phys.* **A757**, 28 (2005);  
I. Arsene *et al.* [BRAHMS Collaboration], *Nucl. Phys.* **A757**, 1 (2005).
- [4] B. Jacak, talk at this Conference.
- [5] D. Kharzeev, *Acta Phys. Pol. B* **37**, 3205 (2006) these proceedings.
- [6] J.P. Blaizot, F. Gelis, *Nucl. Phys.* **A750**, 148 (2005).
- [7] J. Jalilian-Marian, Y. Kovchegov, *Prog. Part. Nucl. Phys.* **56**, 104 (2006).
- [8] I.M. Dremin, J.W. Gary, *Phys. Rep.* **349**, 301 (2001).
- [9] E.A. De Wolf, I.M. Dremin, W. Kittel, *Phys. Rep.* **270**, 1 (1996).
- [10] I. Balitsky, L.N. Lipatov, *Sov. J. Nucl. Phys.* **28**, 822 (1978).
- [11] E.A. Kuraev, L.N. Lipatov, V.S. Fadin, *Sov. Phys. JETP* **45**, 199 (1977).
- [12] H1 Collaboration, *Acta Phys. Pol. B* **33**, 2841 (2002).
- [13] ZEUS Collaboration, *Phys. Lett.* **B345**, 576 (1995).
- [14] S. Forte, G. Altarelli, R.D. Ball, [hep-ph/0606323](#).
- [15] L.V. Gribov, E.M. Levin, M.G. Ryskin, *Phys. Rep.* **100**, 1 (1983).
- [16] A.H. Mueller, J-W. Qiu, *Nucl. Phys.* **B268**, 427 (1986).
- [17] J.P. Blaizot, A.H. Mueller, *Nucl. Phys.* **B289**, 847 (1987).
- [18] A.H. Mueller, Lectures given at the International Summer School on Particle Production Spanning MeV and TeV Energies (Nijmegen 99), Nijmegen, Netherlands, 8-20, Aug 1999, Lisbon 1999, QCD: Perturbative or Nonperturbative?, pp. 180–209, e-print [[hep-ph/9911289](#)].
- [19] L.D. McLerran, R. Venugopalan, *Phys. Rev.* **D49**, 2233 (1994).
- [20] L.D. McLerran, R. Venugopalan, *Phys. Rev.* **D49**, 3352 (1994).
- [21] L.D. McLerran, R. Venugopalan, *Phys. Rev.* **D50**, 2225 (1994).
- [22] Yu.V. Kovchegov, *Phys. Rev.* **D54**, 5463 (1996).

- [23] S. Jeon, R. Venugopalan, *Phys. Rev.* **D70**, 105012 (2004).
- [24] S. Jeon, R. Venugopalan, *Phys. Rev.* **D71**, 125003 (2005).
- [25] J. Jalilian-Marian, A. Kovner, L.D. McLerran, H. Weigert, *Phys. Rev.* **D55**, 5414 (1997).
- [26] J. Jalilian-Marian, A. Kovner, A. Leonidov, H. Weigert, *Nucl. Phys.* **B504**, 415 (1997).
- [27] J. Jalilian-Marian, A. Kovner, A. Leonidov, H. Weigert, *Phys. Rev.* **D59**, 014014 (1999).
- [28] J. Jalilian-Marian, A. Kovner, A. Leonidov, H. Weigert, *Phys. Rev.* **D59**, 034007 (1999).
- [29] J. Jalilian-Marian, A. Kovner, A. Leonidov, H. Weigert, Erratum. *Phys. Rev.* **D59**, 099903 (1999).
- [30] E. Iancu, A. Leonidov, L.D. McLerran, *Nucl. Phys.* **A692**, 583 (2001).
- [31] E. Iancu, A. Leonidov, L.D. McLerran, *Phys. Lett.* **B510**, 133 (2001).
- [32] E. Ferreira, E. Iancu, A. Leonidov, L.D. McLerran, *Nucl. Phys.* **A703**, 489 (2002).
- [33] I. Balitsky, *Nucl. Phys.* **B463**, 99 (1996).
- [34] Yu.V. Kovchegov, *Phys. Rev.* **D61**, 074018 (2000).
- [35] L.D. McLerran, *Lect. Notes Phys.* **583**, 291 (2002) [[hep-ph/0104285](#)].
- [36] E. Iancu, A. Leonidov, L.D. McLerran, [hep-ph/0202270](#).
- [37] E. Iancu, R. Venugopalan, *Quark Gluon Plasma 3*, eds. R.C. Hwa, X.N. Wang, World Scientific, 2003, p. 249 [[hep-ph/0303204](#)].
- [38] L. McLerran, *Acta Phys. Pol. B* **37**, 3237 (2006); S. Munier, *Acta Phys. Pol. B* **37**, 3451 (2006); G. Soyez, *Acta Phys. Pol. B* **37**, 3477 (2006) — these proceedings.
- [39] D.N. Triantafyllopoulos, *Acta Phys. Pol. B* **36**, 3593 (2005).
- [40] A.M. Stasto, *Acta Phys. Pol. B* **35**, 3069 (2004).
- [41] A. Kovner, *Acta Phys. Pol. B* **36**, 3551 (2005).
- [42] A. Kovner, L.D. McLerran, H. Weigert, *Phys. Rev.* **D52**, 3809 (1995).
- [43] A. Kovner, L.D. McLerran, H. Weigert, *Phys. Rev.* **D52**, 6231 (1995).
- [44] Yu.V. Kovchegov, D.H. Rischke, *Phys. Rev.* **C56**, 1084 (1997).
- [45] A. Krasnitz, R. Venugopalan, *Nucl. Phys.* **B557**, 237 (1999).
- [46] A. Krasnitz, R. Venugopalan, *Phys. Rev. Lett.* **84**, 4309 (2000).
- [47] A. Krasnitz, R. Venugopalan, *Phys. Rev. Lett.* **86**, 1717 (2001).
- [48] A. Krasnitz, Y. Nara, R. Venugopalan, *Nucl. Phys.* **A727**, 427 (2003).
- [49] A. Krasnitz, Y. Nara, R. Venugopalan, *Phys. Rev. Lett.* **87**, 192302 (2001).
- [50] T. Lappi, *Phys. Rev.* **C67**, 054903 (2003).
- [51] F. Gelis, K. Kajantie, T. Lappi, *Phys. Rev.* **C71**, 024904 (2005).
- [52] F. Gelis, K. Kajantie, T. Lappi, *Phys. Rev. Lett.* **96**, 032304 (2006).

- [53] P. Romatschke, R. Venugopalan, *Phys. Rev. Lett.* **96**, 062302 (2006); *Eur. Phys. J.* **A29**, 71 (2006).
- [54] P. Romatschke, R. Venugopalan, *Phys. Rev.* **D74**, 045011 (2006).
- [55] E.S. Weibel, *Phys. Rev. Lett.* **2**, 83 (1959).
- [56] F. Gelis, R. Venugopalan, *Nucl. Phys.* **A776**, 135 (2006).
- [57] F. Gelis, R. Venugopalan, *Nucl. Phys.* **A779**, 177 (2006).
- [58] G. t'Hooft, M.J.G. Veltman, CERN report 73-9.
- [59] M.J.G. Veltman, *Physica* **29**, 186 (1963).
- [60] S.K. Kauffmann, M. Gyulassy, *J. Phys. A* **11**, 1715 (1978).
- [61] I. Dremin, private communication.
- [62] V.A. Abramovsky, V.N. Gribov, O.V. Kancheli, *Sov. J. Nucl. Phys.* **18**, 308 (1974).
- [63] C. Itzykson, J.B. Zuber, *Quantum Field Theory*, McGraw-Hill 1980.
- [64] J. Schwinger, *J. Math. Phys.* **2**, 407 (1961).
- [65] L.V. Keldysh, *Sov. Phys. JETP* **20**, 1018 (1964).
- [66] A.J. Baltz, F. Gelis, L.D. McLerran, A. Peshier, *Nucl. Phys.* **A695**, 395 (2001).
- [67] J. Berges, I.O. Stamatescu, *Phys. Rev. Lett.* **95**, 202003 (2005).
- [68] N. Armesto, L. McLerran, C. Pajares, [hep-ph/0607345](#).
- [69] T. Lappi, L. McLerran, *Nucl. Phys.* **A772**, 200 (2006).
- [70] D. Kharzeev, A. Krasnitz, R. Venugopalan, *Phys. Lett.* **B545**, 298 (2002).
- [71] E. Shuryak, *Nucl. Phys.* **A715**, 289 (2003) [[hep-ph/0205031](#)].
- [72] H. Kowalski, D. Teaney, *Phys. Rev.* **D68**, 114005 (2003).
- [73] D. Kharzeev, E. Levin, M. Nardi, *Phys. Rev.* **C71**, 054903 (2005).
- [74] A. Carati, L. Galgani, *Physica* **A280**, 106 (2000).
- [75] T. Lappi, [hep-ph/0606207](#).
- [76] D. Kharzeev, M. Nardi, *Phys. Lett.* **B507**, 121 (2001).
- [77] D. Kharzeev, E. Levin, *Phys. Lett.* **B523**, 79 (2001).
- [78] J.-Y. Ollitrault, *Phys. Rev.* **D46**, 229 (1992).
- [79] T. Lappi, R. Venugopalan, [nucl-th/0609021](#).
- [80] T. Hirano, U.W. Heinz, D. Kharzeev, R. Lacey, Y. Nara, *Phys. Lett.* **B636**, 299 (2006).
- [81] H.-J. Drescher, A. Dumitru, A. Hayashigaki, Y. Nara, *Phys. Rev.* **C74**, 044905 (2006).
- [82] H.-J. Drescher, Y. Nara, [nucl-th/0611017](#).
- [83] R. Baier, A.H. Mueller, D. Schiff, D.T. Son, *Phys. Lett.* **B502**, 51 (2001).
- [84] A.H. Mueller, *Nucl. Phys.* **B572**, 227 (2000); *Phys. Lett.* **B475**, 220 (2000).
- [85] J. Bjorker, R. Venugopalan, *Phys. Rev.* **C63**, 024609 (2001).
- [86] Z. Xu, C. Greiner, *Phys. Rev.* **C71**, 064901 (2005).

- [87] P. Arnold, J. Lenaghan, G.D. Moore, *J. High Energy Phys.* **0308**, 002 (2003); P. Arnold, J. Lenaghan, G.D. Moore, L.G. Yaffe, *Phys. Rev. Lett.* **94**, 072302 (2005).
- [88] A.H. Mueller, A.I. Shoshi, S.M.H. Wong, *Phys. Lett.* **B632**, 257 (2006).
- [89] P. Romatschke, M. Strickland, *Phys. Rev.* **D68**, 036004 (2003); *Phys. Rev.* **D70**, 116006 (2004).
- [90] S. Mrówczyński, *Phys. Lett.* **B214**, 587 (1988); *Phys. Lett.* **B314**, 118 (1993); *Phys. Lett.* **B363**, 26 (1997); J. Randrup, S. Mrówczyński, *Phys. Rev.* **C68**, 034909 (2003); S. Mrówczyński, *Acta Phys. Pol. B* **37**, 427 (2006).
- [91] P. Arnold, J. Lenaghan, *Phys. Rev.* **D70**, 114007 (2004).
- [92] A. Rebhan, P. Romatschke, M. Strickland, *Phys. Rev. Lett.* **94**, 102303 (2005).
- [93] P. Arnold, G.D. Moore, L.G. Yaffe, *Phys. Rev.* **D72**, 054003 (2005).
- [94] A. Rebhan, P. Romatschke, M. Strickland, *J. High Energy Phys.* **0509**, 041 (2005).
- [95] A. Dumitru, Y. Nara, *Phys. Lett.* **B621**, 89 (2005).
- [96] A. Dumitru, Y. Nara, M. Strickland, [hep-ph/0604149](#).
- [97] B. Schenke, M. Strickland, C. Greiner, M.H. Thoma, *Phys. Rev.* **D73**, 125004 (2006).
- [98] P. Romatschke, A. Rebhan, [hep-ph/0605064](#).
- [99] D. Bödeker, K. Rummukainen, talk by D. Bödeker at the INT workshop on Quark Gluon Plasma Thermalization, Sept. 26th-30th, 2006.
- [100] P. Arnold, G.D. Moore, *Phys. Rev.* **D73**, 025013 (2006); *Phys. Rev.* **D73**, 025006 (2006).
- [101] A.H. Mueller, A.I. Shoshi, S.M.H. Wong, [hep-ph/0607136](#).
- [102] K. Fukushima, F. Gelis, L. McLerran, [hep-ph/0610416](#).
- [103] F. Gelis, T. Lappi, R. Venugopalan, in progress.
- [104] A.H. Mueller, D.T. Son, *Phys. Lett.* **B582**, 279 (2004); S. Jeon, *Phys. Rev.* **C72**, 014907 (2005).
- [105] F. Gelis, S. Jeon, R. Venugopalan, in preparation.
- [106] J. Benecke, T.T. Chou, C.N. Yang, E. Yen, *Phys. Rev.* **188**, 2159 (1969).
- [107] G.J. Alner *et al.*, *Z. Phys.* **C33**, 1 (1986).
- [108] J.E. Elias *et al.*, *Phys. Rev.* **D22**, 13 (1980).
- [109] I.G. Bearden *et al.* [BRAHMS Collaboration], *Phys. Lett.* **B523**, 227 (2001); *Phys. Rev. Lett.* **88**, 20230 (2002).
- [110] B.B. Back *et al.* [PHOBOS Collaboration], *Phys. Rev. Lett.* **91**, 052303 (2003); *Phys. Rev.* **C74**, 021901 (2006) [[nucl-ex/0509034](#)].
- [111] J. Adams *et al.* [STAR Collaboration], *Phys. Rev. Lett.* **95**, 062301 (2005); *Phys. Rev.* **C73**, 034906 (2006).
- [112] F. Gelis, A.M. Stasto, R. Venugopalan, [hep-ph/0605087](#), to appear in *Eur. Phys. J. C*.

- [113] Yu.V. Kovchegov, A.H. Mueller, *Nucl. Phys.* **B529**, 451 (1998).
- [114] A. Dumitru, L.D. McLerran, *Nucl. Phys.* **A700**, 492 (2002).
- [115] D. Kharzeev, Yu.V. Kovchegov, K. Tuchin, *Phys. Rev.* **D68**, 094013 (2003).
- [116] J.P. Blaizot, F. Gelis, R. Venugopalan, *Nucl. Phys.* **A743**, 13 (2004).
- [117] J.P. Blaizot, F. Gelis, R. Venugopalan, *Nucl. Phys.* **A743**, 57 (2004); F. Gelis, R. Venugopalan, *Phys. Rev.* **D69**, 014019 (2004).
- [118] H. Fujii, F. Gelis, R. Venugopalan, hep-ph/0603099; *Phys. Rev. Lett.* **95**, 162002 (2005).
- [119] K. Tuchin, *Phys. Lett.* **B593**, 66 (2004); Yu.V. Kovchegov, K. Tuchin, *Phys. Rev.* **D74**, 054014 (2006).
- [120] N.N. Nikolaev, W. Schafer, *Phys. Rev.* **D71**, 014023 (2005); N.N. Nikolaev, W. Schafer, B.G. Zakharov, *Phys. Rev. Lett.* **95**, 221803 (2005).
- [121] F. Gelis, Y. Mehtar-Tani, *Phys. Rev.* **D73**, 034019 (2006).
- [122] J. Jalilian-Marian, *Phys. Rev.* **C70**, 027902 (2004).
- [123] M. Hirai, S. Kumano, M. Miyama, *Phys. Rev.* **D64**, 034003 (2001); M. Hirai, S. Kumano, T.-H. Nagai, *Phys. Rev.* **C70**, 044905 (2004); K.J. Eskola, V. Kolhinen, C. Salgado, *Eur. Phys. J.* **C9**, 61 (1999); D. De Florian, R. Sassot, *Phys. Rev.* **D69**, 074028 (2004).
- [124] M.A. Braun, *Eur. Phys. J.* **C16**, 337 (2000); hep-ph/0010041; N. Armesto, M.A. Braun, *Eur. Phys. J.* **C20**, 517 (2001).
- [125] E. Gotsman, E.M. Levin, M. Lublinsky, U. Maor, *Nucl. Phys.* **A696**, 851 (2001); *Eur. Phys. J.* **C27**, 411 (2003); E. Levin, M. Lublinsky, *Nucl. Phys.* **A696**, 833 (2001); M. Lublinsky, *Eur. Phys. J.* **C21**, 513 (2001).
- [126] K. Golec-Biernat, L. Motyka, A.M. Staśto, *Phys. Rev.* **D65**, 074037 (2002).
- [127] J.L. Albacete, N. Armesto, J.G. Milhano, C.A. Salgado, U.A. Wiedemann, *Phys. Rev.* **D71**, 014003 (2005).
- [128] K. Rummukainen, H. Weigert, *Nucl. Phys.* **A739**, 183 (2004).
- [129] K. Golec-Biernat, M. Wusthoff, *Phys. Rev.* **D59**, 014017 (1999).
- [130] I. Balitsky, *Phys. Rev.* **D 72**, 074027 (2005).
- [131] C. Albajar *et al.*, UA1 Collaboration, *Nucl. Phys.* **B335**, 261 (1990).
- [132] B.A. Kniehl, G. Kramer, B. Potter, *Nucl. Phys.* **B 582**, 514 (2000).
- [133] A. Szczurek, *Acta Phys. Pol. B* **34**, 3191 (2003).
- [134] D. Kharzeev, E. Levin, M. Nardi, *Nucl. Phys.* **A730**, 448 (2004), Erratum *Nucl. Phys.* **A743**, 329 (2004).
- [135] B.B. Back *et al.* [PHOBOS Collaboration], *Phys. Rev.* **C70**, 061901(R) (2004).